

# Pristine Dwarf-Galaxy Survey I: A detailed photometric and spectroscopic study of the very metal-poor Draco II satellite.

Nicolas Longeard<sup>1</sup>, Nicolas Martin<sup>1,2</sup>, Else Starckenburg<sup>3</sup>, Rodrigo A. Ibata<sup>1</sup>, Michelle L. M. Collins<sup>4,6</sup>, Marla Geha<sup>6</sup>, Benjamin P. M. Laevens<sup>5</sup>, R. Michael Rich<sup>7</sup>, David S. Aguado<sup>8,9</sup>, Anke Arentsen<sup>3</sup>, Raymond G. Carlberg<sup>10</sup>, Patrick Côté<sup>11</sup>, Vanessa Hill<sup>12</sup>, Pascale Jablonka<sup>13,14</sup>, Jonay I. González Hernández<sup>8,9</sup>, Julio F. Navarro<sup>15</sup>, Rubén Sánchez-Janssen<sup>11,16</sup>, Eline Tolstoy<sup>17</sup>, Kim A. Venn<sup>15</sup>, Kris Youakim<sup>3</sup>

<sup>1</sup> *Université de Strasbourg, CNRS, Observatoire astronomique de Strasbourg, UMR 7550, F-67000 Strasbourg, France*

<sup>2</sup> *Max-Planck-Institut für Astronomy, Königstuhl 17, D-69117, Heidelberg, Germany*

<sup>3</sup> *Leibniz Institute for Astrophysics Potsdam (AIP), An der Sternwarte 16, 14482 Potsdam, Germany*

<sup>4</sup> *Department of Physics, University of Surrey, Guildford, GU2 7XH, Surrey, UK*

<sup>5</sup> *Institute of Astrophysics, Pontificia Universidad Católica de Chile, Av. Vicua Mackenna 4860, 7820436 Macul, Santiago, Chile*

<sup>6</sup> *Department of Astronomy, Yale University, New Haven, CT 06520, USA*

<sup>7</sup> *University of California Los Angeles, Department of Physics & Astronomy, Los Angeles, CA, USA*

<sup>8</sup> *Instituto de Astrofísica de Canarias, Via Lactea, 38205 La Laguna, Tenerife, Spain*

<sup>9</sup> *Universidad de La Laguna, Departamento de Astrofísica, 38206 La Laguna, Tenerife, Spain*

<sup>10</sup> *Department of Astronomy & Astrophysics, University of Toronto, Toronto, ON M5S 3H4, Canada*

<sup>11</sup> *NRC Herzberg Astronomy and Astrophysics, 5071 West Saanich Road, Victoria, BC V9E 2E7, Canada*

<sup>12</sup> *Laboratoire Lagrange, Université de Nice Sophia-Antipolis, Observatoire de la Côte d'Azur, CNRS,*

*Bd de l'Observatoire, CS 34229, 06304 Nice cedex 4, France*

<sup>13</sup> *GEPI, Observatoire de Paris, PSL Research University, CNRS, Place Jules Janssen, 92190 Meudon, France*

<sup>14</sup> *Laboratoire d'astrophysique, École Polytechnique Fédérale de Lausanne (EPFL), Observatoire, 1290 Versoix, Switzerland*

<sup>15</sup> *Dept. of Physics and Astronomy, University of Victoria, P.O. Box 3055, STN CSC, Victoria BC V8W 3P6, Canada*

<sup>16</sup> *Royal Observatory Edinburgh, Blackford Hill, Edinburgh, EH9 3HJ, UK*

<sup>17</sup> *Kapteyn Astronomical Institute, University of Groningen, Landleven 12, 9747AD Groningen, Netherlands*

17 May 2022

## ABSTRACT

We present a detailed study of the faint Milky Way satellite Draco II (Dra II) from deep CFHT/MegaCam broadband  $g$  and  $i$  photometry and narrow-band metallicity-sensitive CaHK observations, along with follow-up Keck II/DEIMOS multi-object spectroscopy. Forward modeling of the deep photometry allows us to refine the structural and photometric properties of Dra II: the distribution of stars in colour-magnitude space implies Dra II is old ( $13.5 \pm 0.5$  Gyr), very metal poor, very faint ( $L_V = 180_{-72}^{+124} L_\odot$ ), and at a distance  $d = 21.5 \pm 0.4$  kpc. The narrow-band, metallicity-sensitive CaHK Pristine photometry confirms this very low metallicity ( $[\text{Fe}/\text{H}] = -2.7 \pm 0.1$  dex). Even though our study benefits from a doubling of the spectroscopic sample size compared to previous investigations, the velocity dispersion of the system is still only marginally resolved ( $\sigma_{v_r} < 5.9$  km s<sup>-1</sup> at the 95 per cent confidence level) and confirms that Dra II is a dynamically cold stellar system with a large recessional velocity ( $\langle v_r \rangle = -342.5_{-1.2}^{+1.1}$  km s<sup>-1</sup>). We further show that the spectroscopically confirmed members of Dra II have a mean proper motion of  $(\mu_\alpha^*, \mu_\delta) = (1.26 \pm 0.27, 0.94 \pm 0.28)$  mas/yr in the Gaia DR2 data, which translates to an orbit with a pericenter and an apocenter of  $20.9_{-0.9}^{+0.7}$  and  $184.5_{-134.6}^{+356.4}$  kpc, respectively. Taken altogether, these properties favour the scenario of Dra II being a potentially disrupting dwarf galaxy. The low-significance extra-tidal features we map around the satellite tentatively support this scenario.

**Key words:** galaxies: Dwarf – galaxies: individual: Draco II – Local Group

## 1 INTRODUCTION

During the last decades, important photometric surveys such as the Sloan Digital Sky Survey (York et al. 2000, SDSS), the Panoramic Survey Telescope And Rapid Response System, Pan-STARRS1 (Chambers et al. 2016, PS1), or the Dark Energy Survey (The Dark Energy Survey Collaboration 2005, DES) have led to the discovery of dozens of Milky Way satellites. Some of these systems are extremely faint (e.g., Belokurov et al. 2007; Bechtol et al. 2015; Drlica-Wagner et al. 2015; Kim et al. 2015; Koposov et al. 2015b; Laevens et al. 2015; Martin et al. 2015), but studying them is important in order to better constrain the low-mass end of the galaxy mass function (Koposov et al. 2009). Moreover, systems confirmed to be dwarf galaxies are thought to be among the most dark matter dominated systems in the universe, potentially making them one of the best locations to test the standard cosmological model  $\Lambda$ CDM (e.g., Bullock & Boylan-Kolchin 2017).

However, the distinction between dwarf galaxies and globular clusters can be challenging (e.g. Willman & Strader 2012; Laevens et al. 2014) yet crucial. In the  $\Lambda$ CDM model, dwarf galaxies are located in massive dark matter halos. Thus, they have deep potential wells that can leave a trail of indirect observational evidence. For instance, they are more extended for a given luminosity, which explains the low surface-brightness nature of those systems and why deep photometric surveys were needed to reveal their existence. Dwarf galaxies are overall dynamically hot (i.e. their velocity dispersion is larger than that implied by the mass stored in their baryons alone, Martin et al. e.g., 2007; Simon & Geha e.g., 2007), thus implying the presence of a much higher mass than can be estimated from their stars alone, while the typical velocity dispersion for faint clusters is of order tenths of  $\text{km s}^{-1}$ . Dwarf galaxies also share a few chemical properties: they are overall more metal-poor than old globular clusters with the same luminosity, and show evidence of a large metallicity spread, which indicates that the system has undergone chemical enrichment (Willman & Strader 2012; Kirby et al. 2013). This is a strong indirect evidence for the presence of a dark matter halo as the deeper potential well of dwarf galaxies allows them to retain their gas more efficiently against supernovae winds and shields them against reionization, therefore allowing for the formation of successive stellar populations through time, despite early star formation truncation (e.g., Brown et al. 2014). On the contrary, most Milky Way globular clusters show very low metallicity dispersion with  $\sigma_{[\text{Fe}/\text{H}]} < 0.1$  (Willman & Strader 2012 and references therein). The few clusters with significant enrichment, such as  $\omega$  Cen, are massive systems and even thought to be dwarf galaxy remnants (Bellazzini et al. 2008; Carretta et al. 2010).

As the detection of fainter satellites enabled by deeper and deeper surveys continues, the line between dwarf galaxies and globular clusters becomes blurred. For this reason, dwarf galaxy candidates have to be studied thoroughly: deep observations in both photometry and spectroscopy are needed to constrain the main chemical and structural properties of a given system.

Draco II (Dra II) is a Milky Way satellite discovered by Laevens et al. (2015) in the Pan-STARRS1  $3\pi$  survey. At the time of its discovery, the satellite was found to be

compact (half-light radius  $r_h = 19_{-6}^{+8}$  pc). Martin et al. (2016a) carried out the spectroscopic follow-up of Dra II and inferred a marginally resolved velocity dispersion of  $\sigma_{vr} = 2.9 \pm 2.1 \text{ km s}^{-1}$ . Visual comparison of spectra of the few brightest Dra II member stars suggested that the satellite could be metal poor ( $[\text{Fe}/\text{H}] < -2.1$ ) and could exhibit a metallicity spread. Martin et al. (2016a) tentatively favoured Dra II being a dwarf galaxy, but pointed out that the velocity dispersion of the system is only marginally resolved. Furthermore, no bright giant stars ( $g < 19$ ) were identified as Dra II members, making the estimate of the chemical properties of the satellite challenging. Due to the particular faintness of the satellite, and the small number of bright members, kinematic evidence for a DM halo was limited.

In this work, we reanalyze Dra II and present a detailed study of its properties based on deep photometric observations obtained with the Megacam wide-field imager on the Canada-France-Hawaii Telescope (CFHT, Boulade et al. 2003) and Keck II/DEIMOS spectroscopy (Faber et al. 2003) that complements the sample of Martin et al. (2016a). In particular, we include here novel narrow-band photometry that focuses on the metallicity-sensitive CaHK doublet. We use these observations, which are part of a specific dwarf-galaxy programme within the larger Pristine survey (Starkenburg et al. 2017), to identify the metal-poor Dra II stars and estimate the metallicity and metallicity dispersion of the system.

The paper is arranged as follows: Section 2 describes the observations and data of both our photometry and spectroscopy; Section 3 focuses on the analysis of the deep broadband  $g$  and  $i$  photometry to infer the structural and photometric properties of Dra II; Section 4 specifically centers on the study of the narrow-band CaHK observations to derive the metallicity and metallicity dispersion of the system; and Section 5 revises the multi-object spectroscopic study of Dra II. The paper concludes with a discussion and conclusions in Section 6.

## 2 OBSERVATIONS AND DATA

### 2.1 Photometry

The photometry used in this paper was observed with the wide-field imager MegaCam on CFHT. It consists of deep, broadband observations with  $g_{\text{MC}}$  (487 nm) and  $i_{\text{MC}}$  (770 nm) Megacam filters and narrow-band observations with the new narrow-band CaHK Pristine filter that focuses on the metallicity-sensitive Calcium H&K lines. This is the same filter that is used by the Pristine survey (Starkenburg et al. 2017) to build a metallicity map of the Milky Way halo and search for the most metal-poor stars in the Galaxy. The data for Dra II, which were observed before the official start of the Pristine survey, are now folded into a dedicated effort by the Pristine collaboration to observe all northern, faint Milky-Way dwarf galaxies or dwarf-galaxy candidates with this filter (the Pristine dwarf-galaxy survey).

Observations were conducted in service mode by the CFHT staff during the night of April 5th, 2016 during conditions of good seeing ( $\sim 0.5\text{--}0.7''$ ). Multiple sub-exposures were observed in each band to better address CCD defects

and facilitate cosmic ray removal. Exposure times amounted to  $3 \times 700$  s,  $5 \times 500$  s, and  $3 \times 705$  s in the  $g_{MC}$ ,  $i_{MC}$ , and CaHK bands, respectively. After retrieval from the CFHT archive, the images are processed with a version of the Cambridge Astronomical Survey Unit pipeline (Irwin & Lewis 2001), which is specifically tailored to MegaCam data. We refer the reader to Ibata et al. (2014) for more details. The astrometric solution is derived using the catalogue of Pan-STARRS1 stars (PS1; Chambers et al. 2016) that are located in the field and have uncertainties on the  $g_{P1}$  PS1 photometry lower than 0.1 mag. The astrometric solution is good at the  $\sim 0.1''$  level.

MegaCam  $g_{MC}$  and  $i_{MC}$  bands are then transformed onto the PS1 photometric system by using the PS1  $g_{P1}$  and  $i_{P1}$  catalogues. Unsaturated MegaCam point sources are cross identified with PS1 sources having photometric uncertainties below 0.05 mag. To derive the colour equations between the instrumental and PS1 magnitudes, we performed a second-order polynomial fit. We find

$$\begin{aligned} g_{MC} - g_{P1} &= a_0^g x^2 + a_1^g x + a_2^g, \\ i_{MC} - i_{P1} &= a_0^i x^2 + a_1^i x + a_2^i, \end{aligned}$$

with  $x \equiv g_{MC} - i_{MC}$ . The calibration yields  $a_0^g = -0.0208 \pm 0.0021$ ,  $a_1^g = 0.0626 \pm 0.0051$ ,  $a_2^g = 3.5304 \pm 0.0052$  for the  $g$  band and  $a_0^i = -0.0235 \pm 0.0019$ ,  $a_1^i = -0.0235 \pm 0.0048$ ,  $a_2^i = 4.2369 \pm 0.0047$  for the  $i$  band. The uncertainties on the polynomials coefficients are propagated into the photometric uncertainties. For clarity, we drop the P1 subscripts in the rest of the text.

The narrow-band CaHK photometry is processed following the treatment presented in the paper describing the Pristine survey and includes specific calibration steps to deal with variations in the photometry as a function of the position in the field of view (Starkenburger et al. 2017). The Pristine model that translates ( $CaHK$ ,  $g$ ,  $i$ ) into  $[Fe/H]$  is recalculated for the PS1 photometric system and applied to the Draco II photometry.

All MegaCam magnitudes are dereddened following Schlegel, Finkbeiner & Davis (1998) and using the extinction coefficients from Schlafly & Finkbeiner (2011), but it is worth noting that Dra II is located in a low extinction area of the sky, with a median  $E(B - V)$  of 0.018 mag. We rely on the CASU flags to isolate point sources. The MegaCam photometry are deeper than the original PS1 photometry that enabled the discovery of Dra II but this means that the MegaCam data saturate for magnitudes brighter than  $i \sim 17.7$ . For this reason, we complement the MegaCam data set with the PS1 photometry for magnitudes brighter than this limit. Finally, we clean the sample from stars for which the information on either of the two broadbands is missing, we discard stars with photometric uncertainties larger than 0.2 mag in either of the two bands, and we further discard faint sources with  $g < 24.5$ . This latter cut removes regions of the colour-magnitude diagram (CMD) for which the star/galaxy separation becomes inefficient and the data are contaminated by a large number of background compact galaxies.

The final photometric sample comprises 12,638 stars with broadband photometry, out of which 3,238 also have good quality  $CaHK$  magnitudes. The spacial distribution of a fraction of this sample, composed only of Dra II-like

stars, is shown in the left panel of Figure 1, where the system is clearly visible as a compact stellar overdensity.

## 2.2 Spectroscopy

Dra II was observed during two different runs using the Deep Extragalactic Imaging Multi-Object Spectrograph (DEIMOS) in multi-object spectroscopy mode: a first mask was observed in 2015 and was the focus of the study presented by Martin et al. (2016a) whilst the second run was observed a year later on September 4th, 2016. We used our group's standard set-up for these observations, employing the OG550 filter, the 1200 lines  $\text{mm}^{-1}$  grating and a central wavelength of  $7800 \text{ \AA}$ . This results in a FWHM resolution at our central wavelength of  $\sim 1.3 \text{ \AA}$ , and covers a wavelength range of  $\sim 6500 - 9000 \text{ \AA}$ . Such a setup allows us to well-resolve the Ca II triplet lines at  $\sim 8500 \text{ \AA}$ . These strong absorption features are used to measure the line-of-sight velocities of our observed stars. The mask was observed for 1 hour, split into  $3 \times 1200$  seconds exposures.

Stars were selected for targeting using the colour-magnitude diagram for Dra II and they were given a priority for observation based on their distance from a fiducial isochrone, which highlighted the main sequence turn-off (MSTO), sub-giant and red giant branch of Dra II. We then designed a slitmask using the IRAF DSIMULATOR software package provided by Keck Observatories. In total, 96 stars were selected for observation, and 73 of these targets returned spectra of sufficiently high  $S/N$  such that a velocity could be measured using the pipeline detailed in Ibata et al. (2011) and Martin et al. (2016a). All stars with a signal-over-noise ratio below 3.0 or a velocity uncertainty greater than  $15 \text{ km s}^{-1}$  were finally discarded. Heliocentric velocities and equivalent widths from stars observed twice are transformed into one single measurement by computing the weighted mean and uncertainties from the two independent velocity measurements. We do not investigate the potential binarity of Dra II stars in great detail as the low signal-over-noise of the spectra translate into typical velocity uncertainties in the range  $5-15 \text{ km s}^{-1}$ , which can make the detection of any variability challenging. Martin et al. (2016a) presented a spectroscopic study of Dra II using the 2015 dataset, however, the heliocentric velocities of the 2015 stars in this work are slightly different: using the usual method of the Ibata et al. (2011) pipeline to derive the velocities, the average difference of the 2015 and 2016 velocities is not  $0 \text{ km s}^{-1}$  as expected, but is shifted of a few  $\text{km s}^{-1}$ . These effects appear when the velocities are derived through a non-flexible, but supposedly more precise method in the pipeline of Ibata et al. (2011), that was used in the paper of Martin et al. (2016a). In this work, using a slightly less precise, but more flexible method of the same pipeline to extract the velocities, we are able to get rid of these systematics and find the expected mean difference in velocities for all stars observed twice of  $0 \text{ km s}^{-1}$ .

## 3 BROADBAND PHOTOMETRY ANALYSIS

The CMD of Dra II for sources within two half-light radii ( $2r_h$ , see below) is presented in Figure 2 (left panel). For

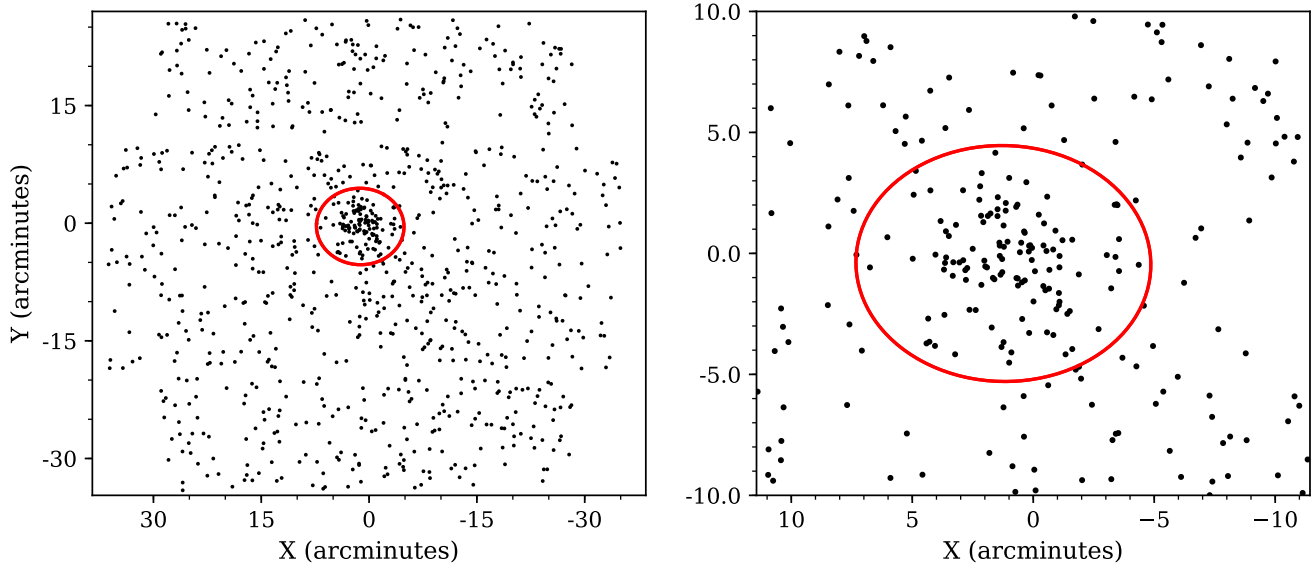


**Figure 1.** *Left panel:* Distribution of MegaCam stars corresponding to a Dra II-like stellar population, centred on the system. The mask selecting Dra II-like stars only is shown in Figure 2. The red line represents the two half-light radii ( $r_h \sim 3.0'$ ,  $\epsilon \sim 0.23$ ) region of Dra II based on the favoured model found in section 3. *Right panel:* Magnified view of the central region.

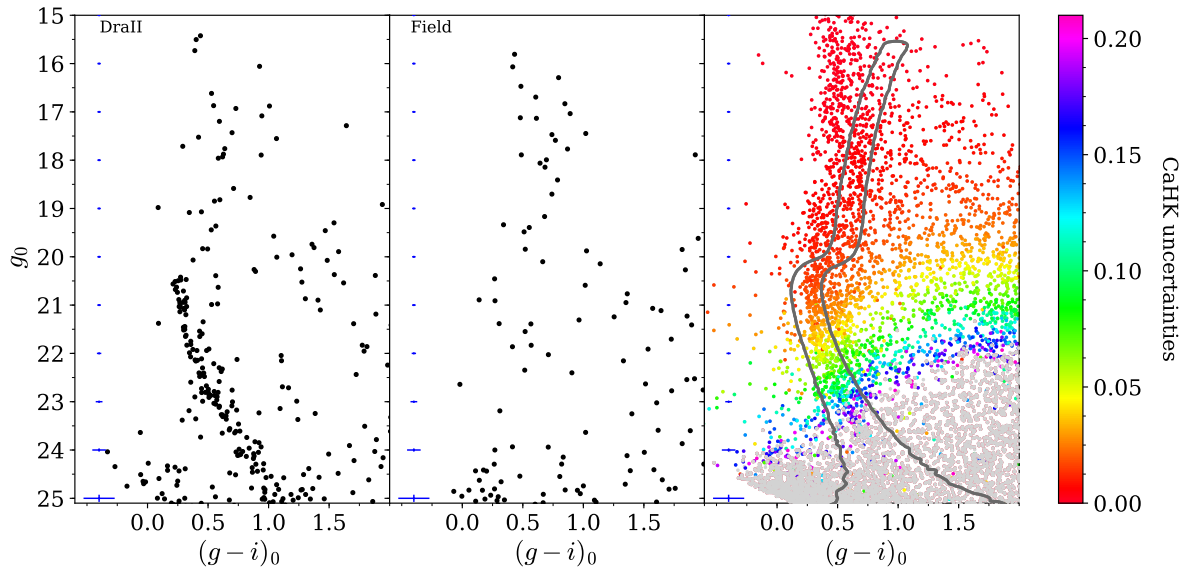


**Figure 2.** *Left panel:* CMD of stars within two half-light radii ( $r_h \sim 3.0'$ ) of the Dra II centroid. The main sequence of Dra II clearly stands out and points towards an old and metal-poor stellar population. The satellite seems to have very few, if any, giant stars. The photometric uncertainties in the  $g$  band and  $g - i$  colour are shown every magnitude on the left of each panel. *Middle panel:* The field CMD obtained within a similarly sized region  $\sim 25$  arcminutes away from Dra II centroid. *Right panel:* CMD of all stars in the photometric dataset, colour-coded according to the  $CaHK$  photometric uncertainties. Stars coloured in grey have  $CaHK$  uncertainties above 0.2. The  $CaHK$  is clearly shallower than the broadband  $g$  and  $i$  photometry. Finally, the mask selecting only Dra II-like stellar population is shown in solid, dark-grey line.

comparison, the CMD of a field region of the same coverage but selected in the outskirts of the MegaCam field of view is shown in the middle-left panel. The main sequence observed in the Dra II CMD is consistent with an old and metal-poor stellar population (see below) as originally

pointed out by Laevens et al. (2015), but the MegaCam data is much deeper and traces the main sequence of the system more than three magnitudes below the turnoff. The exquisite MegaCam CMD is highlighted by the narrowness of this sequence. The 50 per cent completeness of the data

in the  $g$  band is reached at  $g = 25.2$  mag and  $i = 23.9$  mag. We confirm that the main sequence of Dra II contains very few stars brighter than the turnoff and that the satellite is particularly faint. Anticipating on the spectroscopic analysis presented below, the right panel of Figure 15 highlights stars with radial velocity measurements. Likely Dra II members appear in red with  $v_r \sim -345$  km s<sup>-1</sup>. With these velocities, it is possible to isolate a handful of potential Dra II stars just above the turnoff. We find no bright RGB stars and no horizontal branch stars in the system.

### 3.1 Structural and CMD analysis

We take advantage of the deep MegaCam data and of the better sampling of the system to revisit the structural analysis performed by Laevens et al. (2015). The analysis is based heavily on the algorithm presented in Martin, de Jong & Rix (2008) and Martin et al. (2016b) and we separately infer the CMD-properties of Dra II. Altogether, we aim to estimate the structural properties of the system (the coordinate offsets of the centroid from the literature values,  $X_0$  and  $Y_0$ , the half-light radius along the major axis,  $r_h$ , the ellipticity<sup>1</sup>,  $\epsilon$ , the position angle of the major axis east of north,  $\theta$ , and the number of stars within the MegaCam data,  $N^*$ ), along with its distance modulus  $m - M$ , Age  $A$ , metallicity  $[\text{Fe}/\text{H}]_{\text{CMD}}$ , and abundance in  $\alpha$  elements  $[\alpha/\text{Fe}]$ .

For any star  $k$  in our sample, the pieces of information used at this stage are the coordinates of the star  $X_k$  and  $Y_k$ , projected on the sky on the plane tangent to Dra II's centroid, and the MegaCam magnitudes,  $g_k$  and  $i_k$ . For clarity, we define  $\vec{d}_k^{sp} \equiv \{X_k, Y_k\}$  and  $\vec{d}_k^{CMD} \equiv \{g_k, i_k\}$ . The suite of parameters we aim to infer is divided into a set of structural parameters  $\mathcal{P}_{sp} \equiv \{X_0, Y_0, r_h, \epsilon, \theta, N^*, \eta_{sp}\}$  and a set of CMD-related parameters,  $\mathcal{P}_{CMD} \equiv \{m - M, A, [\text{Fe}/\text{H}]_{\text{CMD}}, [\alpha/\text{Fe}], \eta_{CMD}\}$ , with  $\eta_{sp}$  and  $\eta_{CMD}$  the fractions of Dra II stars in the spacial and CMD data sets. Following these definitions and keeping in mind that any star could be a Dra II star or a field star that belongs to the Milky-Way contamination, we can express the spacial likelihood of star  $k$  as

$$\ell_{sp}^{tot}(\vec{d}_{k,sp}|\mathcal{P}_{sp}) = \eta_{sp}\ell_{sp}^{\text{DraII}}(\vec{d}_{k,sp}|\mathcal{P}_{sp}) + (1 - \eta_{sp})\ell_{sp}^{\text{MW}}(\vec{d}_{k,sp}), \quad (1)$$

where  $\ell_{sp}^{\text{DraII}}$  and  $\ell_{sp}^{\text{MW}}$  are the spacial likelihoods of star  $k$  in the Dra II or the field-contamination models, respectively.

We follow Martin et al. (2016b) and assume that Dra II stars follow an exponential radial density profile whereas the field contamination is taken to be flat over the MegaCam field of view. However, and contrary to Martin et al. (2016b), we assume  $N^*$  is a parameter to be determined by the normalization. For this reason, the formalism is slightly different here. The radial density profile of the system is expressed as

$$\rho_{\text{dwarf}}(r) = \frac{1.68^2}{2\pi r_h^2(1 - \epsilon)} \exp(-1.68 \frac{r}{r_h}), \quad (2)$$

<sup>1</sup> The ellipticity is defined as  $\epsilon = 1 - \frac{a}{b}$ , with  $a$  and  $b$  the major and minor axes of the ellipse respectively.

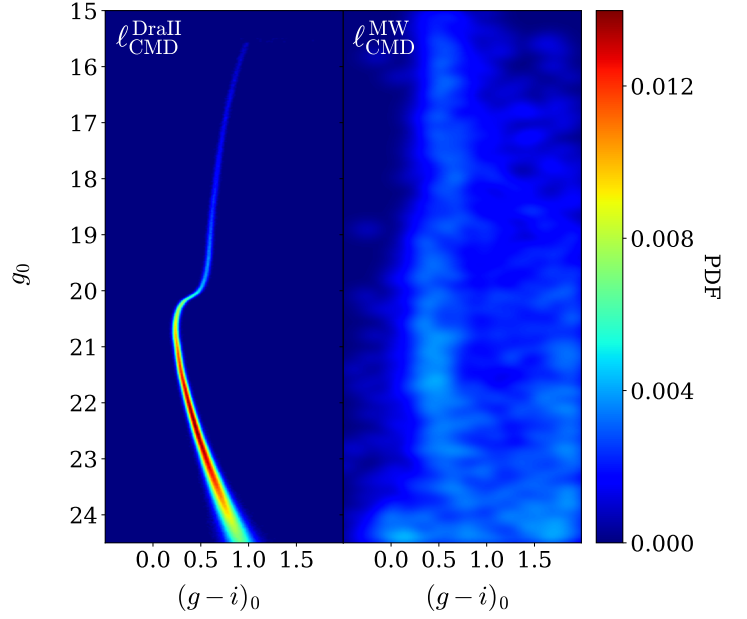


**Figure 3.** *Left panel* : Likelihood of the stellar population favoured by our model ( $A$ : 13.5 Gyr,  $[\text{Fe}/\text{H}]_{\text{CMD}} = -2.4$ ,  $[\alpha/\text{Fe}] = 0.6$  and a distance modulus of 16.67). It is constructed from a theoretical isochrone weighted by its luminosity function, convolved by the typical Megacam photometric uncertainties, and finally weighted by the completeness in  $g_0$  and  $i_0$ . *Right panel*: Likelihood of the contamination stars. The maximum density for the left panel is far greater than for the background likelihood on the right so the two are represented with a square-root colour scale.

with  $r$  the elliptical radius, which relates to projected sky coordinates  $(x, y)$  via

$$r = \left[ \left( \frac{1}{1 - \epsilon} ((X - X_0) \cos \theta - (Y - Y_0) \sin \theta) \right)^2 + \left( (X - X_0) \sin \theta + (Y - Y_0) \cos \theta \right)^2 \right]^{1/2}. \quad (3)$$

The spacial likelihood of the Dra II component of the model is then simply

$$\ell_{sp}^{\text{DraII}}(X_k, Y_k) = \frac{\rho_{\text{dwarf}}(r)}{\int_{\mathcal{A}} \rho_{\text{dwarf}}(r) d\mathcal{A}}, \quad (4)$$

where  $\mathcal{A}$  is the area of the sky over which the analysis is conducted.

The spacial likelihood of the Milky Way contamination model is much simpler and, with our assumption that it is constant, we simply have

$$\ell_{sp}^{\text{MW}} = \frac{1}{\int_{d\mathcal{A}}}. \quad (5)$$

Similarly, one can express the total CMD likelihood as followed :

$$\ell_{CMD}^{tot}(\vec{d}_{k,CMD}|\mathcal{P}_{CMD}) = \eta_{CMD}\ell_{CMD}^{\text{DraII}}(\vec{d}_{k,CMD}|\mathcal{P}_{CMD}) + (1 - \eta_{CMD})\ell_{CMD}^{\text{MW}}(\vec{d}_{k,CMD}), \quad (6)$$

where  $\ell_{\text{CMD}}^{\text{DraII}}$  and  $\ell_{\text{CMD}}^{\text{MW}}$  are the CMD likelihoods of star  $k$  in the Dra II or the field-contamination models, respectively.

To build the CMD models, we rely on a set of isochrones for Dra II and build an empirical model for the field contamination. We base our CMD model of Dra II,  $\ell_{\text{CMD}}^{\text{DraII}}$ , on a set of Dartmouth isochrones and luminosity functions<sup>2</sup> (Dotter et al. 2008) calculated for the PS1 photometric system. For a given set of CMD parameters  $\mathcal{P}_{\text{CMD}}$ , we download the isochrone and luminosity function (LF) of the stellar population of this age  $A$ , metallicity  $[\text{Fe}/\text{H}]_{\text{CMD}}$ , and  $\alpha$  abundance  $[\alpha/\text{Fe}]$ , and shift it by the distance modulus  $m - M$ . Since the isochrones and LFs provided by the Dartmouth library are not continuous but discrete tracks, they are linearly splined. The isochrones are then weighted according to their associated LF. At this stage, each isochrone is a continuous track in CMD space with a ‘height’ equal to the luminosity function along it. We then generate a CMD PDF of where the system stars are likely to be located by simply convolving this track with the photometric uncertainties. With this formalism, we implicitly assume that Dra II contains a single stellar population and any intrinsic spread in the properties of the system will generate wider posterior PDFs. However, as isochrones pile up towards the blue in the metal-poor end regime ( $[\text{Fe}/\text{H}] < -1.4$ ), only significant metallicity or age gradients would affect our results. Finally, the colour-magnitude space over which the PDF is calculated is implemented with pixel sizes of 0.01 magnitude on the side, so we further convolve the resulting PDF by a Gaussian of dispersion 0.01 mag to avoid aliasing issues in our representation of the PDF. Since this PDF is supposed to describe the observed Dra II features of the CMD, the completeness of the data needs to be taken into account, therefore, each track is weighted by the product of the completenesses in  $g_0$  and  $i_0$ . This completeness is computed following the model built by Martin et al. (2016b) on similar MegaCam data, simply shifted to the appropriate reference median magnitude (the median magnitude of all stars in our photometry with photometric uncertainties between 0.09–0.11). The final step normalizes this PDF to unity so it is properly defined. An example of the resulting model is shown in the left-hand panel of Figure 3 for the specific set of parameters  $\mathcal{P}_{\text{CMD}} = \{m - M = 16.67, A = 13.5 \text{ Gyr}, [\text{Fe}/\text{H}]_{\text{CMD}} = -2.4, [\alpha/\text{Fe}] = +0.6\}$ .

The model for  $\ell_{\text{CMD}}^{\text{MW}}$  is built empirically from the CMD position of field stars in the MegaCam data. We select all stars beyond  $5r_h$  and bin them in CMD space. Each bin has a width of 0.01 mag along both the magnitude and the colour directions. In order to diminish the amount of shot noise in the resulting binned CMD, we further smooth it with a Gaussian kernel of width 0.1 mag in both dimensions. The resulting smoothed CMD is presented in Figure 3 after its normalization so it is a properly defined PDF.

With the model being entirely defined, we can now focus on the inference on the model’s parameters. Since the structural side of the analysis can be biased by the presence of the chip gaps visible in Figure 1, they are accounted for by constructing a binary mask correcting the effective area of the field. From the  $N_{\text{tot}}$  stars present in this region, the

spatial likelihood  $\mathcal{L}_{\text{sp}}$  (resp. for the CMD) of a given model is

$$\mathcal{L}_{\text{sp}} \left( \{\vec{d}_{k,sp}\} | \mathcal{P}_{\text{sp}} \right) = \prod_{k=1}^{N_{\text{tot}}} \ell_{\text{sp}}^{\text{tot}} \left( \vec{d}_{k,sp} | \mathcal{P}_{\text{sp}} \right) \quad (7)$$

and the posterior probability we are after is, trivially,

$$P_{\text{sp}} \left( \mathcal{P}_{\text{sp}} | \{\vec{d}_{k,sp}\} \right) \propto \mathcal{L}_{\text{sp}} \left( \{\vec{d}_{k,sp}\} | \mathcal{P}_{\text{sp}} \right) P_{\text{sp}}(\mathcal{P}_{\text{sp}}), \quad (8)$$

with  $P_{\text{sp}}(\mathcal{P}_{\text{sp}})$  the combined prior on the model parameters. These priors are listed in Table 3 and are chosen to be uniform for an old stellar population, with distance and structural parameters loosely close to the favoured parameters according to Laevens et al. (2015). Anticipating on section 4, the systemic metallicity of the satellite is found to be  $\langle [\text{Fe}/\text{H}]_{\text{DraII}}^{\text{CaHK}} \rangle = -2.7 \pm 0.1 \text{ dex}$  using the narrow-band, CaHK photometry. This result is used as a Gaussian prior to the CMD analysis.

In order to build the posterior N-dimensional distribution function, we devised our own Markov Chain Monte Carlo code based on a Metropolis-Hastings algorithm (Hastings 1970). To ensure convergence, we aim for an acceptance ratio of  $\sim 25$  per cent and run the algorithm for a few million iterations. Convergence is not an issue for this large number of iterations. Finally, for the CMD analysis, we restrict ourselves to a specific region of the CMD: a visual inspection of the Dra II main sequence in Figure 2 shows that all stars outside  $-0.5 < (g - i)_0 < 2.0$  are contaminants. For this reason, there is no need to take them into account in our analysis, and the following CMD and structural analyses are performed only with stars with  $15 < g_0 < 24.5$ , and  $-0.5 < (g - i)_0 < 2.0$ . The resulting two-dimensional marginalised PDFs are presented in Figure 4 for spatial and 5 for CMD parameters.

Our results are compatible with the ones presented by Laevens et al. (2015) in the discovery paper of Dra II. From the deeper MegaCam data, we confirm the half-light radius of the satellite to be  $r_h = 3.0_{-0.5}^{+0.7} \text{ arcmin}$  (vs.  $2.7_{-0.8}^{+1.0} \text{ arcmin}$  before). Overall, the deeper MegaCam data allows for better constraints with smaller uncertainties on all parameters. The use of a Plummer profile instead of an exponential profile yields similar results. The radial profile of the favoured spatial model is presented in Figure 8.

The CMD part of the analysis yields a robust distance estimate ( $m - M = 16.67 \pm 0.05 \text{ mag}$ ; or a heliocentric distance  $d = 21.5 \pm 0.4 \text{ kpc}$ ) that is slightly smaller than the one proposed by Laevens et al. (2015), who estimated a distance modulus of  $\sim 16.9$  by eye. The favoured isochrone also corresponds to a stellar population of  $A = 13.5 \pm 0.5 \text{ Gyr}$ ,  $[\text{Fe}/\text{H}]_{\text{CMD}} = -2.40 \pm 0.05 \text{ dex}$ , and  $[\alpha/\text{Fe}] = +0.6 \text{ dex}$ . The 1D PDFs of the CMD parameters are shown in Figure 5, while Figure 6 shows that this stellar population is a good description of the features in the CMD of Dra II and of the stars identified as members of the satellite through a spectroscopic study (see section 5). The choice of showing only 1D PDFs for the CMD inference is purely aesthetic: each parameter is chosen over a grid that can have large steps (e.g.  $[\alpha/\text{Fe}]$  is chosen over a grid with 0.2 dex step), which does not give representative or aesthetically pleasing

<sup>2</sup> <http://stellar.dartmouth.edu/models/webtools.html>

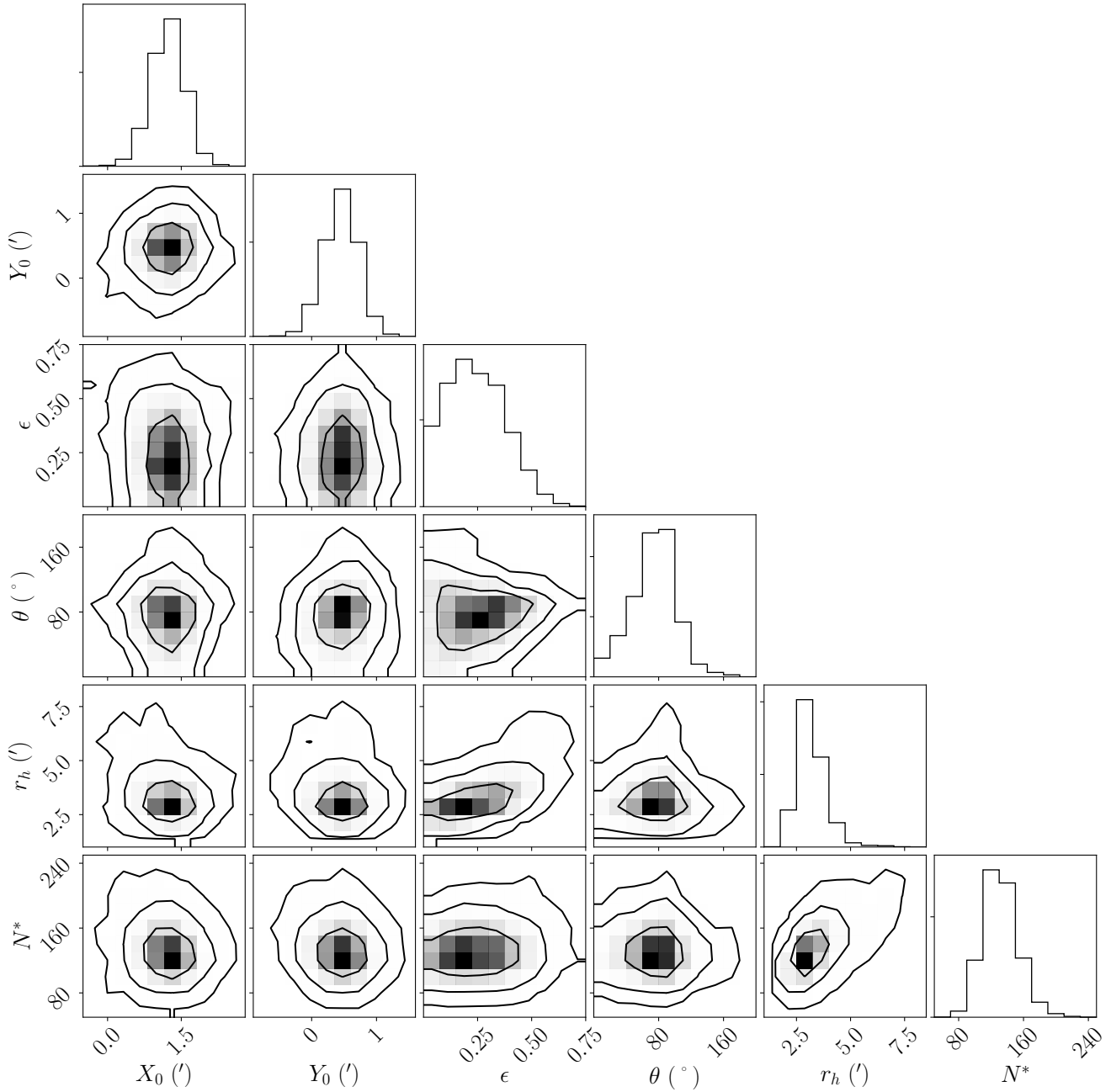


**Figure 4.** One- and two-dimensional posterior PDFs of the structural parameters of Dra II, inferred using the method described in section 3.1. Contours correspond to the usual 1, 2 and  $3\sigma$  confidence intervals in the case of a two-dimensional Gaussian.

2D contours. It is however important to note that there is no clear correlation between the CMD parameters.

The alpha-abundance ratio of the favoured model is to be taken with caution as it reaches the limits of the  $[\alpha/\text{Fe}]$  range allowed by this set of isochrones. The alpha abundance of 0.6 found above is high but not totally unrealistic for a dwarf galaxy: Vargas et al. (2013) shows that faint Milky Way dwarf galaxies such as Segue 1 ( $M_V \sim -1.5$ ) are compatible with this result. Another fit was performed using a uniform prior in  $[\alpha/\text{Fe}]$  over the range  $[0.0, 0.4]$  to test the

analysis without reaching the end of the alpha abundance grid. This does not significantly change our results.

To investigate the impact of the choice of the completeness model used, the favoured CMD and spacial model are used to simulate a Dra II-like population. The analysis is then performed three more times: one time with our actual completeness model, and two other times using the completeness model shifted by  $\pm 0.5$  mag respectively. The results of these analyses are all consistent within the uncer-

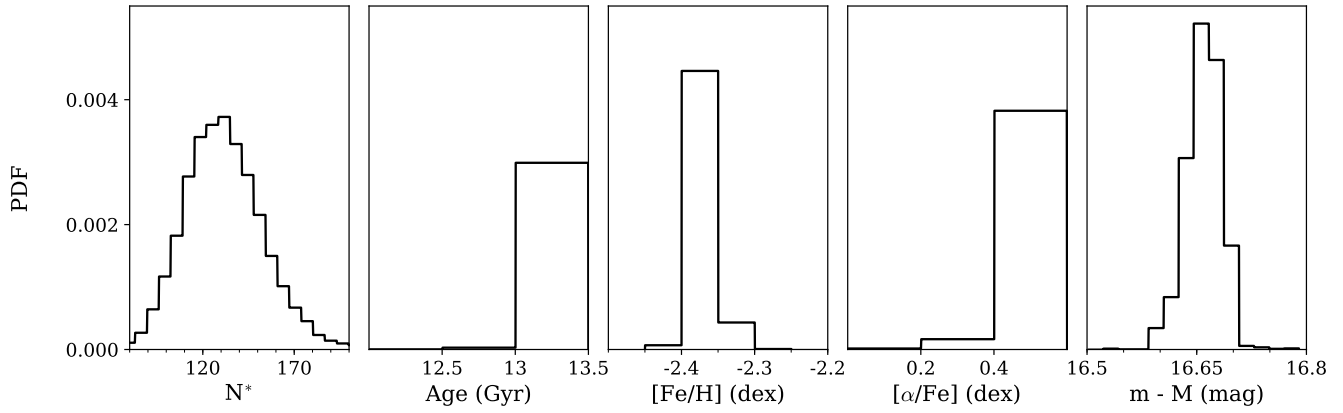


**Figure 5.** One-dimensional PDFs of the CMD parameters of Dra II.

**Table 1.** Inferred properties of Dra II.

Parameter	Unit	Prior	Favoured model	Uncertainties
RA $\alpha$	degrees	—	238.174	$\pm 0.005$
DEC $\delta$	degrees	—	+64.579	$\pm 0.006$
$r_h$	arcmin	$> 0$	3.0	+0.7 -0.5
$r_h$	pc	—	19.0	+4.5 -2.6
$\theta$	degrees	[0,180]	76	+22 -32
$\epsilon$	-	$> 0$	0.23	$\pm 0.15$
Distance modulus	mag	[16.3,17.1]	16.67	$\pm 0.05$
Distance	kpc	—	21.5	$\pm 0.4$
Age	Gyr	[10,13.5]	13.5	$\pm 0.5$
[Fe/H]	dex	—	-2.7	$\pm 0.1$
$\sigma_{[\text{Fe}/\text{H}]}$	dex	$> 0$	Unresolved	$< 0.24$ dex at 95%
[ $\alpha$ /Fe]	dex	[0.0,0.6]	0.6	$> 0.4$ at 89%
$L_V$	$L_{\odot}$	$> 0$	180	+124 -72
$M_V$	mag	—	-0.8	+0.4 -1.0
$\mu_0$	mag arcsec $^{-2}$	—	28.1	$\pm 0.7$
$\langle v_r \rangle$	km s $^{-1}$	—	-342.5	+1.1 -1.2
$\langle v_r \rangle_{gsr}$	km s $^{-1}$	—	-172.0	+1.1 -1.2
$\sigma_{vr}$	km s $^{-1}$	$> 0$	Unresolved	$< 5.9$ km s $^{-1}$ at 95%
$\mu_{\alpha}^*$	mas.yr $^{-1}$	—	0.54	$\pm 0.27$
$\mu_{\delta}$	mas.yr $^{-1}$	—	0.94	$\pm 0.28$

ainties, showing that the impact of the completeness model is limited and that it does not significantly affect our results.

The systemic metallicity of the satellite appears consistent with the luminosity-metallicity relation for DGs and with the analysis previously proposed by Martin et al. (2016a) in a qualitative analysis of their spectra. We repeat the Calcium-triplet equivalent-width analysis of Martin et al. (2016a) for the three low-RGB stars with S/N > 10 that used the Starkeburg et al. (2010) relation. It is worth pointing out that this relation is calibrated for RGB stars. However, Leaman et al. (2013) implies that it can be applied to stars 2 magnitudes below the RGB and give consistent results. The analysis yields a systemic metallicity for Dra II

of  $[\text{Fe}/\text{H}]_{\text{spectro}} = -2.43^{+0.41}_{-0.82}$  dex, which is compatible with our CMD analysis. Due to the lack of bright member stars (the brightest used in this analysis has  $g_0 = 18.8$ ), it is challenging to obtain tight constraints on the spectroscopic metallicity of the satellite.

As a sanity check, the main sequence of Dra II can be compared to the fiducials of old and metal-poor globular clusters constructed by Bernard et al. (2014). A few of those fiducials are overlaid on the CMD of Dra II in Figure 7. From this figure, fiducials in the metallicity ranges  $-2.4 < [\text{Fe}/\text{H}] < -2.0$  and  $-1.8 < [\text{Fe}/\text{H}] < -1.4$  provide good visual match to the Dra II features and its spectroscopically confirmed members (determined in section 5 be-



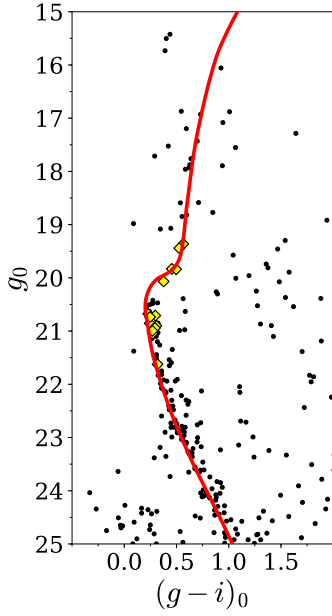


**Figure 6.** CMD of stars within  $2r_h$  of Dra II's centroid, along with the favoured isochrone found in section 3.1, corresponding to a stellar population of  $13.5^{+0.5}_{-1.0}$  Gyr,  $[\text{Fe}/\text{H}]_{\text{CMD}} = -2.40 \pm 0.05$  dex and  $[\alpha/\text{Fe}] = +0.6$  dex. Stars confirmed as spectroscopic members in section 5 are represented as yellow diamonds.

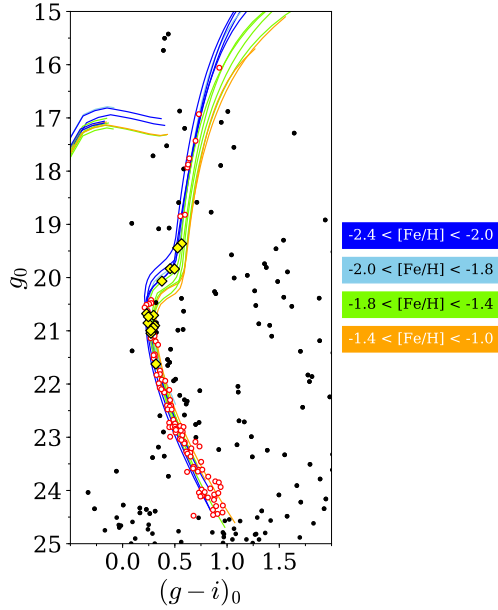


**Figure 7.** CMD of stars within two half-light radii of Dra II centroid. Several metal-poor globular cluster fiducials from Bernard et al. (2014) are represented and colour-coded by metallicity ranges. Red circled dots are stars with a Dra II membership probability greater than 1 per cent. Yellow diamonds are Dra II members confirmed by spectroscopy. The fiducials that best represent the Dra II CMD features are the blue ones, with a metallicity range  $-2.4 < [\text{Fe}/\text{H}] < -2.0$ .

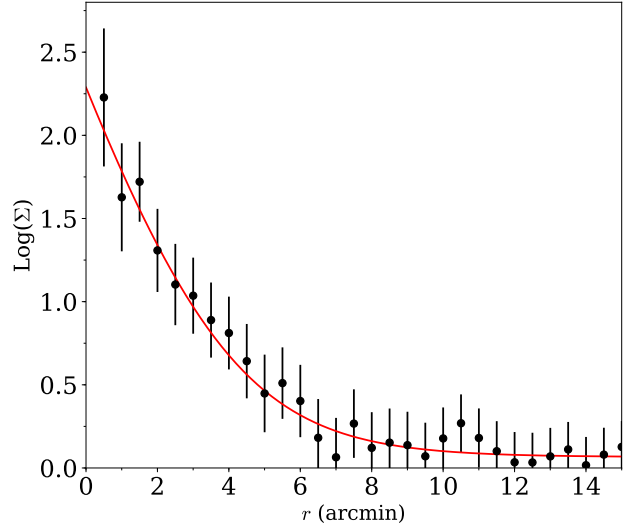


**Figure 8.** Comparison of the favoured exponential radial density profile (red solid line) with the binned data in elliptical annuli following the favoured structural model (dots). The error bars represent Poisson uncertainties on the number count of each annulus.  $r$  is the elliptical radius.

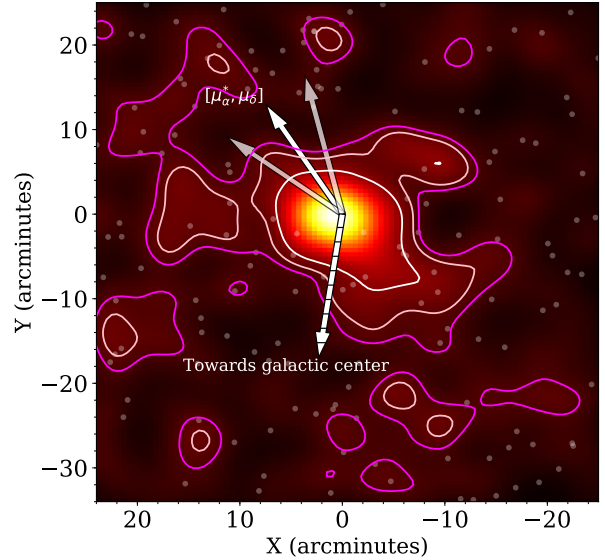


**Figure 9.** On-sky density plot of the full field of view for all stars with  $\mathcal{P}_{mem} \geq 0.01$ , smoothed using a 2 arcminutes gaussian kernel. Regions with a density within the upper 68, 95 and 99.85 per cent of the background pixels distribution are shown with magenta, pink, and white contours respectively. The dashed arrow shows the direction towards the Galactic center. The upper white arrow shows the favoured proper motion vector  $\vec{\mu} = [\mu_{\alpha}^{*, \text{DraII}}, \mu_{\delta}^{\text{DraII}}]$  (see section 6 for more details), while the uncertainties on this vector are shown as the two shaded arrows. Transparent white dots represent bright stars ( $g_0 < 17$ ) over the field.

low and highlighted in yellow in the figure). The most metal-poor fiducials, however, provide a better match for stars with  $P_{mem} > 0.01$  brighter than  $g_0 = 19$  mag. Although this does not give any precise quantitative information on the metallicity of Dra II, it confirms the metallicity measured from the CMD-fitting procedure and from spectroscopy.

Our spacial and CMD models can be used to estimate the Dra II membership for each star by computing the ratio of the satellite likelihood,  $\mathcal{L}_{DraII}(\vec{d})$ , over the total likelihood  $\mathcal{L}_{DraII}(\vec{d}) + \mathcal{L}_{MW}$ . These membership probabilities are reported in Table 3 for all stars in the spectroscopic sample. The membership probability can also be used to draw the density map of the Dra II-like stellar population. The field is binned with intervals of width 0.5 arcminutes in both X and Y. For each bin, we count the density of stars. The map is further convolved with a gaussian kernel of 2 arcminutes. To identify potential structures, the distribution of background pixels, i.e. pixels located further than  $4.0r_h$ , is fitted with a gamma distribution. Pixels with a density within the upper 68, 95, and 99.85 per cent of the total background pixels are represented with magenta, pink, and white contours in Figure 9. This map tentatively reveals the existence of an extended Dra II-like structure over the field of view, consistent with the orientation of the major axis of the satellite. This hint of extra-tidal features could be the sign that Dra II could be tidal disrupting. The orbit of Dra II we infer in section 6 is consistent with the direction of these potential tails. We stress that this needs to be confirmed with a spectroscopic search for members in these regions.

Finally, we investigate the presence of mass segregation within the system as this phenomenon can occur in globular clusters, but not in dwarf galaxies, and could therefore be used as a diagnostic for the nature of the satellite (Kim et al. 2015). The stellar population models provided by the Dartmouth library give an estimate of the mass of a given star following these isochrones. Using this piece of information, each star within  $3r_h$  is associated with its most likely mass by comparison with the favoured isochrone. This subsample is then separated into three mass ranges ( $0.5 - 0.6M_\odot$ ,  $0.6 - 0.7M_\odot$ , and  $0.7 - 0.8M_\odot$ ). The cumulative number of stars in each mass range with respect to their radial distance to Dra II is finally computed. This procedure is repeated for stars with a membership probability above 1, 35 and 50 per cent respectively to investigate the potential effect of the contamination on the analysis. The results are shown in Figure 10 for the 35 per cent case. This analysis gives no conclusive evidence of mass segregation in the satellite. Choosing a membership probability threshold of 1 and 50 per cent does not change significantly the results.

### 3.2 Luminosity and absolute magnitude $M_V$

We rely on the method presented in Martin et al. (2016a) to determine the total luminosity of the satellite: this method uses the PDFs on the stellar population of Dra II and on the number of stars within the MegaCam data,  $N^*$ , to infer the total luminosity of the system. Therefore, it does not correspond to the sum of the fluxes of all stars seemingly members of Dra II in the observed CMD, but it can be seen as a statistical determination of the luminosity of a system with the structural and CMD properties of Dra II.

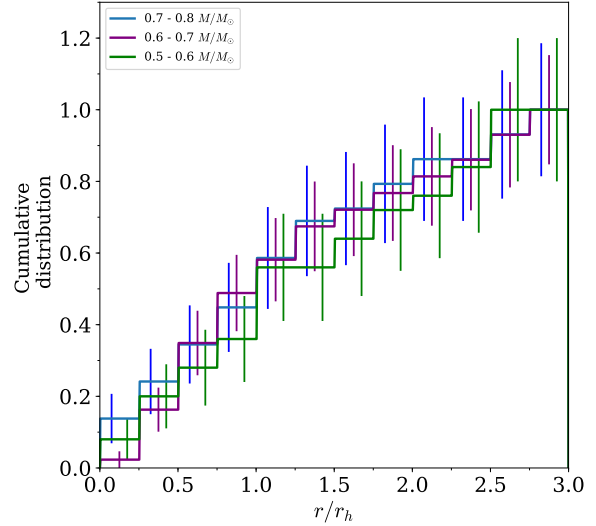


**Figure 10.** Normalised cumulative number of stars from 0 to 3 half-light radii, for three mass intervals :  $0.8-0.7M_\odot$  (blue),  $0.7-0.6M_\odot$  (purple) and  $0.6-0.5M_\odot$  (green). The analysis is performed for all stars with a CMD membership probability above 35 per cent.

At every iteration in the procedure, we randomly draw a target  $N_j^*$  value from the  $N^*$  PDF, as well as a set of stellar parameters ( $A_j$ ,  $[\alpha/\text{Fe}]_j$ ,  $[\text{Fe}/\text{H}]_{\text{CMD},j}$ ,  $(m - M)_j$ ) from the PDFs obtained through the inference of section 3.1. CMD stars are then simulated according to the  $j$ -th stellar population. The probability to draw a star at a given magnitude  $g_0$  is given by the luminosity function. For each simulated star, its colour  $(g - i)_0$  and magnitude  $g_0$  are checked. If they fall within the CMD box used to perform the fit in the previous section, it is flagged. The simulated star is then independently checked against the completeness of the data in both  $g$  and  $i$ . The  $g$  and  $i$  values are then converted into a  $V$  magnitude using the colour equations presented in Tonry et al. (2012). Once the number of flagged simulated stars is equal to  $N_j^*$ , the flux of all stars, flagged or not, is summed to yield the total luminosity,  $L_{V,j}$ , of that realization of the satellite. Those luminosity values are then converted into absolute magnitudes,  $M_{V,j}$ . Repeating this exercise several thousands of times yields the PDFs presented in Figure 11.

From this analysis, Dra II emerges as a very faint satellite, with a luminosity of only  $L_V = 180_{-72}^{+124} L_\odot$ , corresponding to an absolute magnitude of  $M_V = -0.8_{-1.0}^{+0.4}$  mag. The satellite has a surface brightness of  $\mu_0 = 28.1 \pm 0.7$  mag.arcsec $^{-2}$ , comparable to the Milky-Way satellites with the lowest surface brightness. Shifting the completeness model by  $\pm 0.5$  mag does not significantly change the inferred luminosity. Most of the simulated CMDs contain no RGB star much brighter than the turnoff, which is compatible with the absence of confirmed RGB stars brighter than  $g_0 = 19.3$  in our spectroscopic sample (Figure 7 and Table 2 for the member list) and with the observed CMD. This value is however significantly fainter than the one of Laevens et al. (2015), who found a luminosity of  $1259_{-758}^{+1903} L_\odot$ . Two possible explanations for this difference can be proposed. First, the photometry at hand in 2015 is 2 magnitudes shallower

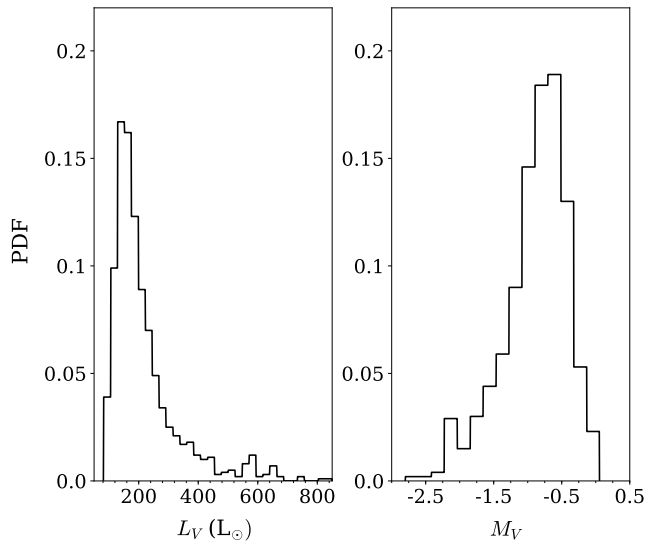


**Figure 11.** PDFs of the V-band luminosity (left panel) and absolute magnitude (right panel) of Dra II. The system is particularly faint, with a favoured luminosity of only  $L_V = 180_{-72}^{+124} L_\odot$ .

than ours, thus only reaching the bright end of the main sequence of Dra II. Finally, a small fraction of our simulated CMDs still predicts the existence of a RGB star in the satellite that could lead to a significant increase in luminosity. This is illustrated by the bright tail up to  $800 L_\odot$  in the left panel of Figure 11 which is only due to the existence of one or two giant stars in a small fraction of our simulated CMDs. One bright star ( $g < 16$ ) in Dra II would potentially be enough to solve the discrepancy between Laevens et al. (2015) and this work. However, recent spectroscopic investigations of bright Dra II candidates did not lead to the identification of any additional member with  $g < 17$ . Therefore, the discrepancy found regarding the luminosity must be caused by an overestimation of the additional overall number of stars by Laevens et al. (2015), driven by shallower and noisier data.

#### 4 NARROW-BAND CAHK ANALYSIS

The Pristine survey (Starkenburg et al. 2017) combines CFHT narrow-band CaHK photometry with broadband colours, typically  $g - i$ , to infer photometric metallicities (hereafter  $[\text{Fe}/\text{H}]_{\text{CaHK}}$ ). A specific set of Pristine observations aims at observing all known northern Milky-Way dwarf galaxy (or dwarf-galaxy candidate) with  $M_V > -9.0$ . These images are much deeper than the usual Pristine observations (1-hour vs. 100-second integrations) but remain shallower than the broadband  $g$  and  $i$  photometry described in section 3. Reliable CaHK photometry, i.e. with  $\text{CaHK}$  uncertainty below 0.1, is achieved down to  $g \sim 23.0$ .

In Figure 12, we show the typical colour-colour space used by the Pristine collaboration, for which stars with  $[\text{Fe}/\text{H}] \sim -1$  or lower reside in the bottom part of the panel and more metal-poor stars towards the top. Comparison via models and calibration onto thousands of stars in common with the Segue spectroscopic survey allow us to

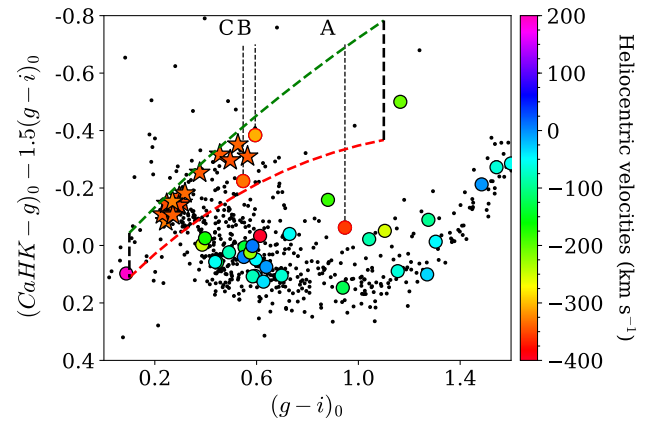


**Figure 12.** Pristine colour-colour diagram. The usual temperature proxy  $(g - i)_0$  is represented on the x-axis while the metallicity information is carried by the  $(\text{CaHK} - g) - 1.5 * (g - i)$  colour shown on the y-axis (see Starkenburg et al. (2017)). Stars observed spectroscopically that pass the  $\text{CaHK}$  quality cut, i.e. an uncertainty on the  $\text{CaHK}$  photometry below 0.1, are colour-coded according to their heliocentric velocities. Small black dots are field stars and form a clear stellar locus of more metal-rich stars ( $[\text{Fe}/\text{H}] \sim -1$  or above) while more metal-poor stars are located towards above this sequence. Two iso-metallicity sequences with  $[\text{Fe}/\text{H}] = -3.5$  and  $[\text{Fe}/\text{H}] = -1.8$  are shown as green and red dashed lines, respectively. Most stars compatible with the velocity of Dra II (red-orange) are located between these two sequences, and form a distinct, more metal-poor population than the rest of the spectroscopic sample made of more metal-rich halo and disc stars. The black dashed lines show a colour cut of  $0.1 < (g - i)_0 < 1.1$ , which is applied to discard potential foreground dwarfs. A, B and C are the three stars close to the Dra II velocity peak that were discarded using the CaHK and CMD cuts (see the text for more detail).

assign a  $[\text{Fe}/\text{H}]_{\text{CaHK}}$  value to all these stars (Starkenburg et al. 2017; Youakim et al. 2017). Two iso-metallicity sequences of respectively  $[\text{Fe}/\text{H}] = -3.5$  (green dashed line) and  $[\text{Fe}/\text{H}] = -1.8$  (red dashed line) are shown in the figure for illustration purposes. In the figure, we also highlight stars that are part of our DEIMOS spectroscopic sample that will be discussed in the next section. The group of likely Dra II members at  $v_r \sim -345 \text{ km s}^{-1}$  mainly clumps along a low metallicity sequence that is compatible with the low metallicity inferred from the broadband photometry.

The Starkenburg et al. (2017) Pristine metallicity model tends to slightly underestimate the metallicity at the low-metallicity end. Therefore, before turning to the Dra II CaHK data, we first estimate and correct for this bias when determining a  $[\text{Fe}/\text{H}]_{\text{CaHK}}$ . We use the same catalogue Starkenburg et al. (2017) used to build their  $(\text{CaHK}, g, i)$  to  $[\text{Fe}/\text{H}]_{\text{CaHK}}$  model, with the same quality criteria on the Pristine photometry and SEGUE/SDSS spectra. We bin this sample of 3,999 stars into 0.2 dex bins in metallicity for stars in the interval  $-4.0 < [\text{Fe}/\text{H}]_{\text{CaHK}} < -1.0$ . For each of these bins, we determine the median value of both  $[\text{Fe}/\text{H}]_{\text{SEGUE}}$  and  $[\text{Fe}/\text{H}]_{\text{CaHK}}$ . The bias is then defined as the difference between these two values. This set of values is then fitted with a third-order polynomial to model

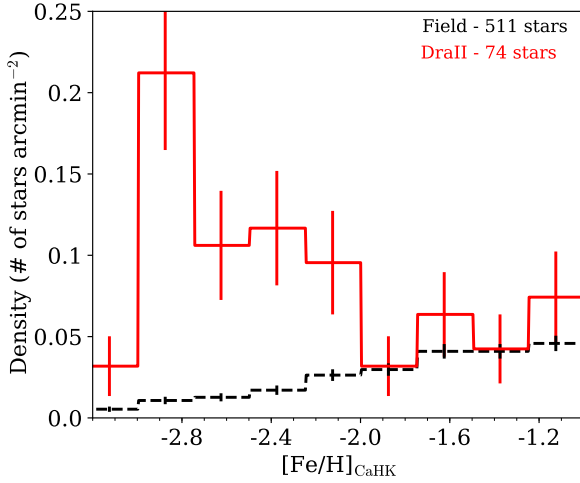


**Figure 13.** Area-normalised metallicity distribution for all stars within  $2r_h$  (solid red line). The same histogram is also shown for all field stars, i.e. stars outside  $5r_h$  (black dashed line). Dra II members are clearly responsible for an overdensity of stars around  $[\text{Fe}/\text{H}] \sim -2.8$  in the red distribution.

the metallicity bias throughout the whole metallicity range. This bias is, at most, of  $\sim 0.2$  dex at  $[\text{Fe}/\text{H}] \lesssim -2.0$ .

For every star in the Dra II sample with uncertainties on the CaHK magnitude below 0.1, we first apply the model of Starkenburg et al. (2017) to infer a photometric metallicity, which we then correct for the bias modeled above. The area-normalised metallicity distribution for stars within  $2r_h$  of Dra II is shown in red in Figure 13. For comparison, the black-dashed histogram shows the same distribution but for field stars, i.e. for all stars outside  $5r_h$ . Dra II stars stand out quite prominently as a significantly metal-poor overdensity compared to the field contamination. A lot of stars in the figure appear to be at the same photometric metallicity around  $-3.0$ . However, the calibration of the Pristine model becomes unreliable at  $[\text{Fe}/\text{H}]_{\text{CaHK}} \sim -3.0$ . The high number of stars at  $\sim -3.0$  stars is probably a consequence of this.

Using Pristine metallicities, we want to infer both the mean metallicity of the system,  $\langle [\text{Fe}/\text{H}]_{\text{DraII}}^{\text{CaHK}} \rangle$ , and its dispersion  $\sigma_{[\text{Fe}/\text{H}]}$ . In order to do so, we assume that the distribution of photometric metallicities in the Dra II sample corresponds to a Gaussian-distributed Dra II population and a contamination model  $\mathcal{L}_{\text{bkg}}$ , which is constructed empirically from the field data outside a  $5r_h$  radius. The metallicity distribution of this contamination sample is binned, then smoothed with a Gaussian kernel of 0.1 dex to account for poor number counts in some metallicity bins. Finally, we assume the following metallicity distribution model:

$$\mathcal{L}(\{[\text{Fe}/\text{H}]_{\text{CaHK},k}, \delta_{[\text{Fe}/\text{H}],k}\} | \langle [\text{Fe}/\text{H}]_{\text{DraII}}^{\text{CaHK}} \rangle, \sigma_{[\text{Fe}/\text{H}]}) \\ = \prod_k G([\text{Fe}/\text{H}]_{\text{CaHK},k} | \langle [\text{Fe}/\text{H}]_{\text{DraII}}^{\text{CaHK}} \rangle, \sigma_k) + \mathcal{L}_{\text{bkg}}([\text{Fe}/\text{H}]_{\text{CaHK},k}),$$

with  $G(x|\mu, \sigma)$  the value of a Gaussian distribution of mean  $\mu$  and dispersion  $\sigma$  evaluated for  $x$ ,  $\delta_{[\text{Fe}/\text{H}],k}$  the uncertainty on the photometric metallicity of star  $k$ , and  $\sigma_k = \sqrt{\sigma_{[\text{Fe}/\text{H}]}^2 + \delta_{[\text{Fe}/\text{H}],k}^2}$ .

The inference analysis yields the two-dimensional joined PDF of  $\langle [\text{Fe}/\text{H}]_{\text{DraII}}^{\text{CaHK}} \rangle$  and  $\sigma_{[\text{Fe}/\text{H}]}$  presented in Figure 14. The metallicity of the system is found to be  $\langle [\text{Fe}/\text{H}]_{\text{DraII}}^{\text{CaHK}} \rangle = -2.7 \pm 0.1$  dex, with a metallicity dispersion lower than 0.24 dex at the 95% confidence level. The favoured systemic metallicity confirms that Dra II is significantly metal-poor. The fraction of Dra II stars favoured by the analysis is  $\eta \sim 0.6$ , corresponding to a total of 41 stars. The metallicity dispersion of the satellite cannot be resolved with this dataset. Performing the analysis using an asymmetrical gaussian does not change significantly our results.

In order to validate our inference based on the CaHK metallicities, the same analysis is performed on the Pristine data of two metal-poor globular clusters, M15 and M92. Globular clusters are crucial in this case as their metallicity dispersion is expected to be too small to be resolved using purely photometric metallicities and they are a good test of the quality of our constraints on  $\sigma_{[\text{Fe}/\text{H}]}$ . Carretta et al. (2009a, C09) and Carretta et al. (2009b, C09b) showed that both clusters have a similar spectroscopic metallicity, with  $[\text{Fe}/\text{H}]_{\text{C09b}} = -2.34 \pm 0.06$  dex for M15 and  $[\text{Fe}/\text{H}]_{\text{C09}} = -2.35 \pm 0.05$  dex for M92, as well as metallicity dispersions around  $\sim 0.05$ . The application of our inference model to the globular cluster Pristine datasets yields  $\langle [\text{Fe}/\text{H}]_{\text{M15}} \rangle = -2.32 \pm 0.04$  dex and  $\langle [\text{Fe}/\text{H}]_{\text{M92}} \rangle = -2.38 \pm 0.05$  dex, compatible with the values of C09. As expected, the inferred metallicity dispersions are unresolved for both clusters, as can be seen with the coloured contours in Figure 14. The favoured models yields 43 stars for M15 and 25 stars for M92, comparable to the 41 stars studied in Dra II.

The inference on the metallicity mean and dispersion for the two globular clusters is as expected and yields confidence that the CaHK metallicities are reliable. We therefore conclude that Dra II is indeed a very metal-poor satellite and we further note that despite similar numbers of member stars in the three systems, the Dra II metallicity dispersion PDF is wider than that of the clusters, which may hint at a larger metallicity dispersion for Dra II.

## 5 SPECTROSCOPIC ANALYSIS

We now investigate the dynamical properties of the satellite using our spectroscopic data, for which the processing was detailed in section 2.2. Examples of spectra can be found in Figure 4 of Martin et al. (2016a), who display 4 spectra of our 2015 run that are representative of the whole dataset since the 2016 spectroscopic observations were performed under similar conditions and have similar quality. Their spacial and CMD distribution are shown in Figure 15. The histograms of heliocentric velocities for our 2015 and 2016 runs combined are shown in the middle panel of Figure 16.

Dra II stars clearly stand out in Figure 16 as they form a peak around  $-345 \text{ km s}^{-1}$ , as was already pointed out by Martin et al. (2016a) in their initial analysis of the 2015 data set. A broader distribution around  $\sim -45 \text{ km s}^{-1}$  corresponds to stars from the Milky Way disc while Milky Way halo stars are responsible for the sparsely distributed velocities throughout the range shown here. In order to better constrain the dynamical properties of the system, one has

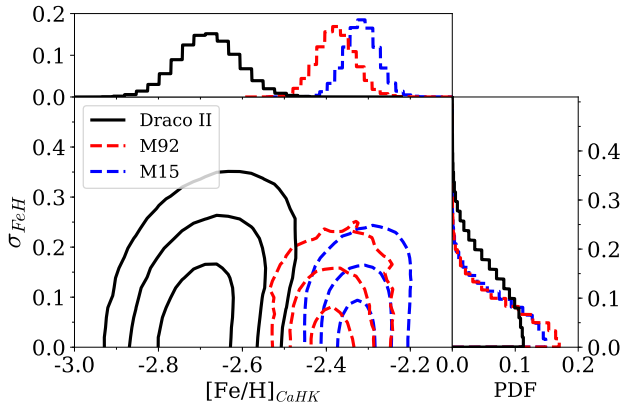


**Figure 14.** Two-dimensional joint PDFs of the systemic CaHK metallicity and its associated dispersion for Dra II (black) and the globular clusters M15 and M92 (blue and red-dashed line, respectively). The marginalised one-dimensional PDFs are shown in the top and right-hand panels for the two parameters. The contours represent the usual 1, 2 and 3 $\sigma$  confidence intervals in the case of a two-dimensional Gaussian distribution.

to isolate Dra II members as well as possible. Particular care should be taken when handling the contamination by Milky Way halo stars that are distributed within a broad velocity range that includes the systemic velocity of the satellite. For this reason, it would not be surprising to find a few contaminating stars in the vicinity of the velocity peak of Dra II. In particular, one can also notice the existence of two slight outliers around the Dra II velocity peak, noted stars A and B. It is quite challenging to know whether those stars are bona fide members based only on their kinematic properties. This is a common problem when dealing with such faint systems for which only a handful of members are confirmed: the velocity dispersion and systemic velocity can be biased by slight outliers that are in fact not members (McConnachie & Côté 2010).

Pristine CaHK photometry can be very useful to clean the spectroscopic sample as the Dra II stellar population is very metal-poor, as shown in section 3.1. All Dra II members are too faint to yield reliable spectroscopic metallicities but it is expected that they can be disentangled from Milky-Way contaminants by using the CaHK photometric metallicities described in the previous section.

The Pristine colour-colour diagram presented in Figure 12 highlights the location of stars with heliocentric velocities, which are colour-coded according to those. As mentioned before, the metal-rich stars from the disc form a clear stellar locus at the bottom of the panel, whereas metal-poor stars are always located above this locus. The two iso-metallicity sequences that bracket the metallicity peak visible in Figure 13, with  $[\text{Fe}/\text{H}] = -3.5$  and  $[\text{Fe}/\text{H}] = -1.8$ , are represented by the green- and red-dashed line, respectively. As expected, stars with velocities compatible with the systemic velocity of Dra II (red-orange) are clearly isolated from the metal-rich, foreground contamination from the Milky Way. Most of the other stars from the spectroscopic sample lie in or close to the metal-rich stellar locus. To help discriminate between Dra II stars and the contamination in our spec-

troscopic sample, we isolate stars with good CaHK photometry ( $\delta_{\text{CaHK}} < 0.1$ ), metallicity uncertainties below 0.3 dex, and, following Figure 13, with  $-3.5 < [\text{Fe}/\text{H}]_{\text{CaHK}} < -1.8$ . Further applying a CMD-cut along the favoured isochrone of section 3.1 yields the cleaned velocity sample that is presented in the bottom panel of Figure 16. It is obvious that the combined CaHK and CMD information has significantly cleaned the velocity distribution, leaving only highly probable Dra II stars. As a result, star A is clearly not a member: not only is it far from the Dra II sequence in the CMD, but it is also far too metal-rich to belong to the system. Star B seems to be at the appropriate photometric metallicity to be a Dra II member but is offset from the Dra II main sequence by 0.1 mag in the CMD. This location corresponds to a part of the CMD where one might expect to find Dra II binary stars (Romani & Weinberg 1991), which could mean that this star is a Dra II member in a binary star and therefore not reliable for the velocity analysis. We also conservatively discard star C for the same reason, even though it falls within the Dra II velocity peak. Keeping star C or discarding it does not change our results on the velocity properties of Dra II. Including B in the sample also has no significant impact as its velocity uncertainty is large ( $\sim 15 \text{ km s}^{-1}$ ).

In order to derive the systemic velocity and velocity dispersion of Dra II from this clean sample, we follow the framework of Martin et al. (2018) and assume stars are normally distributed. The likelihood function is therefore

$$\mathcal{L}(\{v_{r,k}, \delta_{v,k}\} | \langle v_r \rangle, \sigma_v) = \prod_k G(v_{r,k} | \langle v_r \rangle, \sigma_k), \quad (10)$$

with  $G(x|\mu, \sigma)$  the value of a Gaussian distribution of mean  $\mu$  and dispersion  $\sigma$  evaluated on  $x$ ,  $\delta_{v,k}$  the uncertainty on the photometric metallicity of star  $k$  and  $\sigma_k = \sqrt{\sigma_v^2 + \delta_{v,k}^2 + \delta_{v,sys}^2}$ ,  $\delta_{v,sys}$  is the systematic uncertainty floor tied to DEIMOS observations. Here we use the value determined by Martin et al. (2016a,  $\delta_{v,sys} = 2.3 \text{ km s}^{-1}$ ), which is compatible with the value we determine from the few stars in common between the Dra II 2015 and 2016 samples.

The resulting 1D PDFs of the velocity dispersion and systemic velocity are shown in Figure 17. These updated results do not change significantly from those presented by Martin et al. (2016a), despite our slightly larger sample and the removal of dubious members by using the CaHK photometric metallicities. The velocity dispersion of Dra II is only marginally resolved, whereas the inferred systemic velocity is  $\langle v_r \rangle = -342.5^{+1.1}_{-1.2} \text{ km s}^{-1}$ . Assuming a mass-to-light ratio (M/L) of 2 typical of MW globular clusters (McLaughlin & van der Marel 2005), a Dra II-like GC with a size of  $\sim 19 \text{ pc}$  and absolute magnitude of  $\sim -0.8 \text{ mag}$  is expected to have a velocity dispersion of the order of  $\sim 0.25 \text{ km s}^{-1}$  if it is in equilibrium and unaffected by binaries, using the relation of Walker et al. (2009). Therefore, even with a dispersion as small as  $\sim 1 \text{ km s}^{-1}$ , Dra II would still possess a significant amount of DM but, unfortunately, the radial velocities of the 14 members do not constrain the M/L ratio of the satellite.

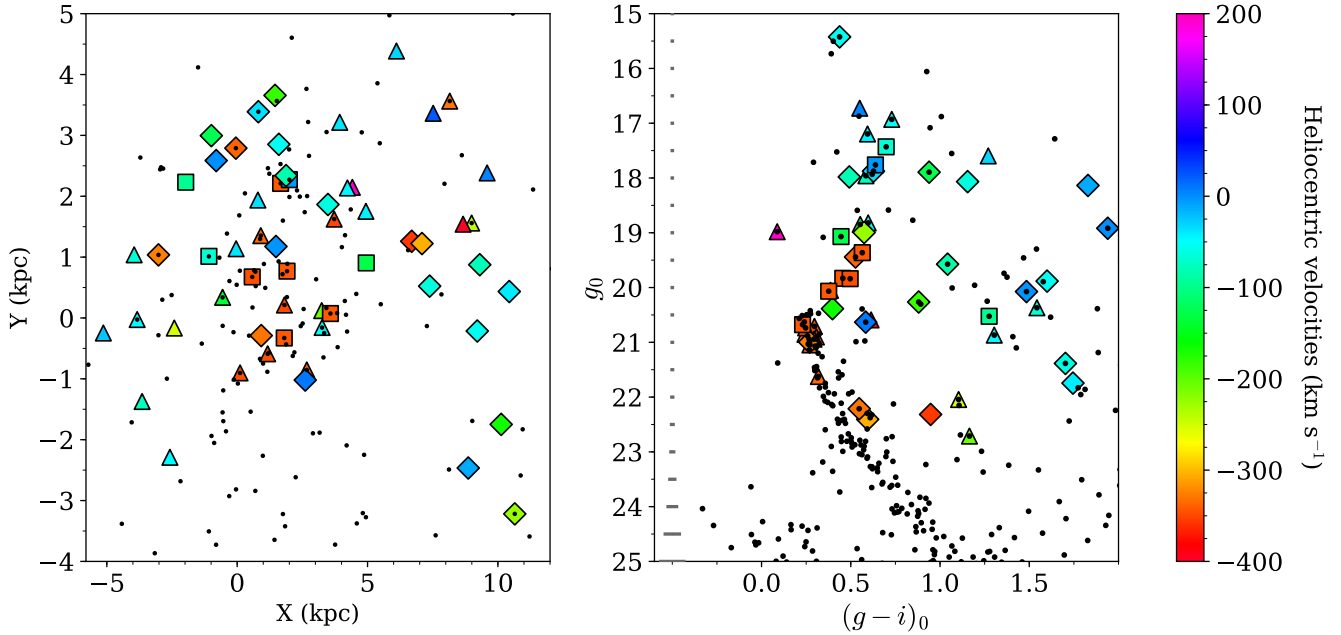


**Figure 15.** *Left panel:* Magnified view of the central region showing the spacial distribution of the spectroscopic sample. Stars observed spectroscopically are represented by large dots colour-coded according to their heliocentric velocities. Diamonds and triangles correspond to stars observed in 2015 and 2016 respectively, while squares correspond to stars observed both in 2015 and 2016. Some of the stars observed spectroscopically do not overlap small black dots as those correspond only to Dra II like population and do not represent the full photometric dataset. *Right panel:* Distribution of the spectroscopic sample in the CMD within two half-light radii of Dra II. Stars lying on the Dra II main sequence, in red-orange, are likely members of the system. Some of the stars with velocity measurements are located further away than 2 half-light radii and thus do not also appear as small dots.

## 6 GAIA DR2 PROPER MOTIONS AND ORBIT

To determine the orbit of Dra II, we extract the proper motions (PMs) of all stars within half a degree from Dra II’s centroid in the Gaia Data Release 2 (Gaia Collaboration et al. 2018a). A cross-match between the 14 identified member stars in section 5 is then performed, resulting in 10 members with a PM measurement. The PMs of the 10 Dra II members are shown in red in Figure 18. The uncertainty-weighted PM of Dra II yields  $\mu_{\alpha}^{*,\text{DraII}} = \mu_{\alpha}^{\text{DraII}} \cos(\delta) = 1.26 \pm 0.27 \text{ mas.yr}^{-1}$  and  $\mu_{\delta}^{\text{DraII}} = 0.94 \pm 0.28 \text{ mas.yr}^{-1}$ , and is shown in Figure 18 as the large, green dot. These measurements take into account the systematic error of  $0.035 \text{ mas.yr}^{-1}$  on the PMs for dSph as shown by Gaia Collaboration et al. (2018b). However, if we instead choose the systematic error presented in that paper for the GCs, our results do not change given the measured uncertainties on  $\mu_{\alpha}^{*,\text{DraII}}$  and  $\mu_{\delta}^{\text{DraII}}$ .

These measurements can be used to put constraints on the orbit of the satellite. To do so, we rely on the GALPY package (Bovy 2015). The MW potential chosen to integrate Dra II orbit is the so-called “MWPotential14” defined within GALPY, constituted of three components: a power-law, exponentially cut-off bulge, a Miyamoto-Nagai potential disk, and a Navarro-Frenk-White DM halo. We integrate 1000 orbits backwards and forwards over 6 Gyr, each time by randomly drawing a position, distance, radial velocity, and PMs from their corresponding PDFs, and extract for each realization the apocenter, pericenter, and ellipticity. The orbit of the favoured model (i.e. favoured position, distance,

radial velocity and PMs) is shown in Figure 19 in the X-Y, X-Z and Y-Z planes, and colour-coded by time. Five random realizations of the orbit are also shown in this figure as partially transparent, grey lines.

This analysis yields a pericenter of  $20.9^{+0.7}_{-0.9} \text{ kpc}$ , an apocenter of  $184.5^{+356.4}_{-134.6} \text{ kpc}$  and an ellipticity of  $0.87^{+0.07}_{-0.08}$ . Dra II seems to be on a quasi-perpendicular orbit with respect to the disk of the MW. Our orbit differs from the one of Simon (2018) who finds that Dra II is on first infall but this is most likely driven by their choice of a light MW ( $0.8 \times 10^{12} M_{\odot}$ ). This is confirmed by the analysis of Fritz et al. (2018). Overall, we are in agreement with the orbital properties of Dra II inferred for the heavy MW by Fritz et al. (2018). Our larger sample nevertheless provides a more stringent constraint on the orbit of Dra II. The fairly elliptical orbit and the small pericenter we infer appear compatible with the idea that the satellite has been severely affected by tides and could explain the low-surface brightness features seen in Figure 9 that roughly align with the PM vector.

## 7 SUMMARY AND DISCUSSION

In this paper, we present an analysis of our deep MegaCam/CFHT broad-band  $g$  and  $i$  photometry of Dra II, combined with narrow-band CaHK photometry from a specific sub-program of the Pristine survey that focuses on all northern sky dwarf-galaxy candidates. We also present an analysis

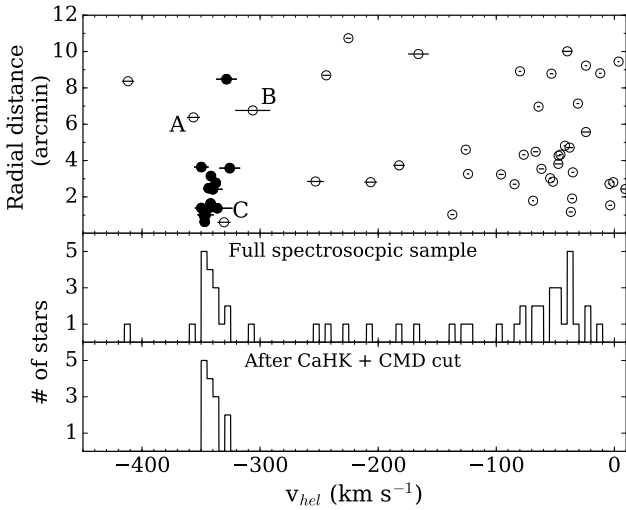


**Figure 16.** *Top panel:* Radial distances to the centroid of Dra II versus heliocentric velocities for all stars in our spectroscopic sample. Black-filled markers represent the remaining spectroscopic population after the CaHK and CMD cuts were applied. They are considered as dynamical members of the system. *Middle panel:* Histogram of the heliocentric velocities in the spectroscopic sample. *Bottom panel:* Histogram of velocities for dynamical member stars only, obtained by discarding stars that do not come out as metal-poor through the CaHK model detailed in section 4 (Figure 12), as well as stars that are not compatible with our favoured CMD model (section 3). They correspond to the black-filled markers in the top panel.

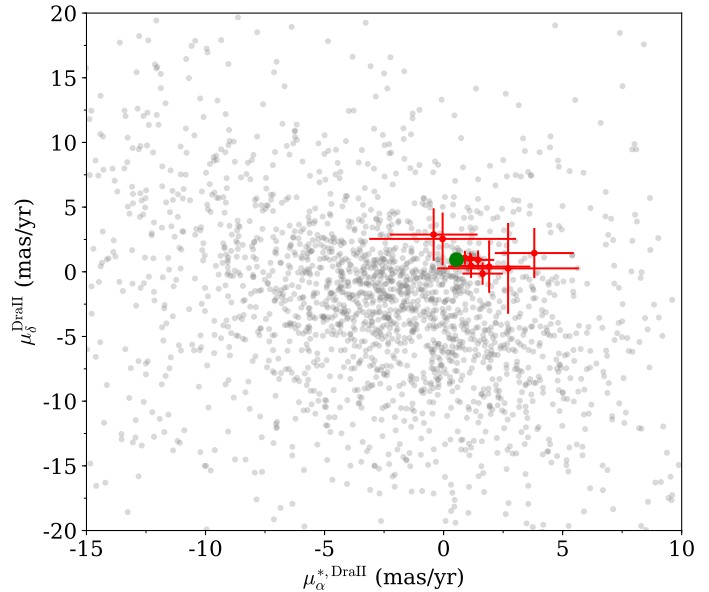


**Figure 18.** PMs in RA and DEC, for field stars (grey) and 10 Dra II dynamical members (red). The mean proper motion of the satellite is represented as a large green dot.

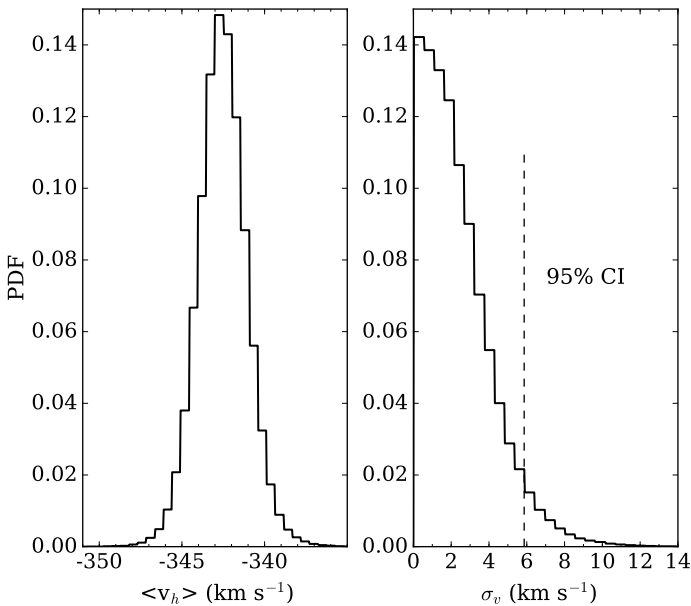


**Figure 17.** Marginalised PDFs for the Dra II systemic velocity (left panel) and velocity dispersion (right panel). The system is dynamically cold, with a marginally resolved velocity dispersion. We constrain the velocity dispersion to be lower than  $5.9 \text{ km s}^{-1}$  at the 95 per cent confidence level (dashed vertical line).

of the extension of our multi-object spectroscopy observed with Keck II/DEIMOS.

We estimate the structural parameters of Dra II and infer properties that are compatible with the previous study of the satellite by Laevens et al. (2015) albeit with smaller uncertainties: the system has a half-light radius of  $r_h = 19.0_{-2.6}^{+4.5}$  pc and is remarkably faint ( $L_V = 180_{-72}^{+124} L_\odot$ ). Based on the CMD information of the observed stars, we confirm that Dra II hosts an old stellar population with an age of  $13.5 \pm 0.5$  Gyr, a metallicity  $[\text{Fe}/\text{H}]_{\text{CMD}} = -2.40 \pm 0.05$  dex,  $[\alpha/\text{Fe}] = +0.6$  dex, and a distance modulus of  $m - M = 16.67 \pm 0.05$  mag. Using the Pristine photometry, we were able to find an estimate of the metallicity of Dra II with  $\langle [\text{Fe}/\text{H}]_{\text{DraII}}^{\text{CaHK}} \rangle = -2.7 \pm 0.1$  dex. This inference is confirmed by the analysis of 3 Dra II spectroscopic members, which yields  $[\text{Fe}/\text{H}]_{\text{spectro}} = -2.43_{-0.82}^{+0.41}$  dex. The metallicity derived from the three different techniques are therefore all consistent. However, the isochrone fitting procedure is limited by the model grid, for which the lowest metallicity is  $-2.45$  dex. Three low-RGB stars were used to derive the spectroscopic metallicity of the satellite using the Calcium triplet relation of Starkenburg et al. (2010). However, this relation is calibrated for RGB stars, though Leaman et al. (2013) shows that it can give consistent results when applied to stars 2 magnitudes fainter. We therefore favour the systemic metallicity inferred by the CaHK technique as it does not suffer from these limitations. The metallicity dispersion of Dra II is only marginally resolved for both the spectroscopic and CaHK procedures. Similarly, applying the same technique to the two old and metal-poor globular clusters M15 and M92 yields no measurable metallicity dispersion, in line with expectations for globular clusters. Fi-

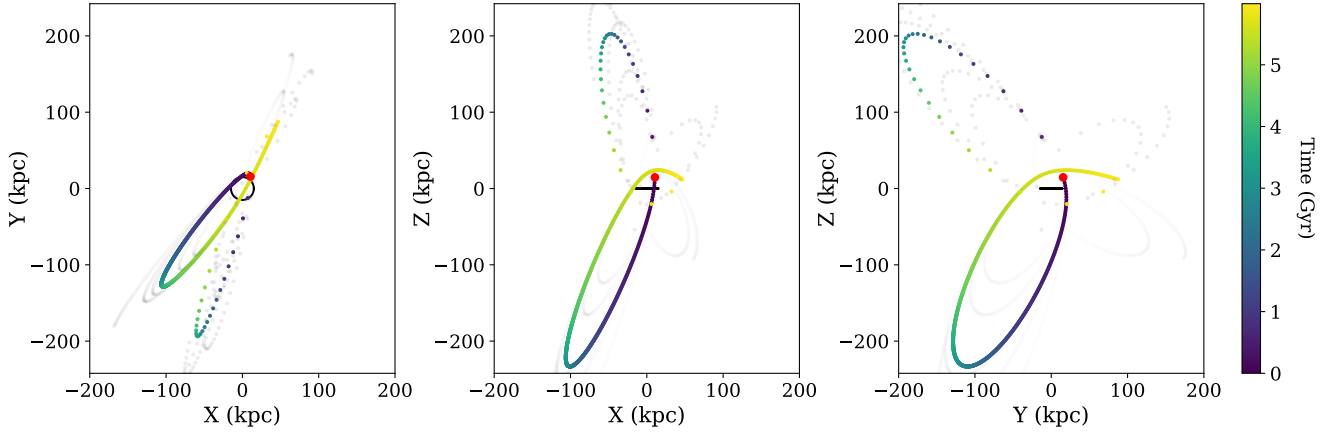


**Figure 19.** Projections of the orbit of Dra II on the X-Y, X-Z and Y-Z planes backwards and forwards over 6.0 Gyr. Six orbits are shown here: the one based on the favoured position, distance, radial velocity and PMs of the satellite, and five others using random realizations of those parameters, as slightly transparent, grey lines. The median orbit is colour-coded according to the time elapsed since present day, in Gyr. Dotted lines represent the backwards-integrated orbits. The current position of Dra II is indicated with a red dot, while the MW disk is shown in black, with a chosen radius of 15 kpc.

nally, we combined the CaHK and broad-band information with our DEIMOS spectroscopy to isolate 14 likely member stars. This sample is used to derive a systemic velocity of  $\langle v_r \rangle = -342.5^{+1.1}_{-1.2} \text{ km s}^{-1}$  and a marginally resolved velocity dispersion, confirming that Dra II is a particularly cold system. Finally, using the Data Release 2 of Gaia, we use 10 Dra II member stars to characterize the orbit of the system: the apocenter and pericenter are found to be  $184.5^{+356.4}_{-134.6} \text{ kpc}$  and  $20.9^{+0.7}_{-0.9} \text{ kpc}$  respectively.

Despite the deep photometry studied here and the additional spectroscopy, the derived properties of Dra II are still challenging to interpret and the nature of the system remains uncertain. Dra II is placed in the general context of Milky Way satellites in Figure 20 and, below, we discuss two broad scenarios: whether Dra II is a globular cluster or a dwarf galaxy.

### 7.1 Is Dra II a globular cluster?

Figure 20 (top-right panel) shows Dra II does not present any clearly constrained dispersion in metallicity, in contrast to confirmed dwarf galaxies. Similarly, dwarf galaxies tend to be dynamically hot whereas the spectroscopic analysis of 14 Dra II members only yields a marginally resolved velocity dispersion. These two properties are compatible with the globular cluster hypothesis.

The globular cluster scenario does not come without difficulties, though. In particular, if the system contains no dark matter, its potential well is entirely determined by its very few stars. Using the formalism of Innanen, Harris & Webbink (1983), the instantaneous tidal radius  $r_t$  of a Milky Way satellite of mass  $M_{\text{cluster}}$  at a distance of  $R$ , is given by

$$r_t = 0.43 \left( \frac{M_{\text{cluster}}}{M_{\text{MW}}} \right)^{1/3} R, \quad (11)$$

with  $M_{\text{MW}}$  the mass of the Milky Way enclosed within that radius  $R$ .

Using Dra II’s galactocentric distance ( $R \sim 23.5 \text{ kpc}$ ) and a cluster mass of  $360 M_{\odot}$ , obtained from the measured luminosity of Dra II and assuming a mass-to-light ratio of 2 (Bell & de Jong 2001), the tidal radius of Dra II is then a mere  $\sim 10 \text{ pc}$ , i.e. much smaller than the extent of a system with a measured half-light radius of  $19.0^{+4.5}_{-2.6} \text{ pc}$ . We would then be observing Dra II just as it is being destroyed by the Milky Way’s tides and, likely, on its final passage around the Galaxy. It would mean that we are observing Dra II during a unique and short-lived moment of its lifetime, and would be a way to explain the relatively high size of the satellite compared to globular clusters of similar faintness : Kim 1 ( $r_h \sim 7 \text{ pc}$ ), Kim 3 ( $r_h \sim 2 \text{ pc}$ ) and Bal 1 ( $r_h \sim 7 \text{ pc}$ ) discovered recently (Conn et al. 2018; Koposov et al. 2007; Luque et al. 2016; Martin et al. 2016c).

Finally, the absence of any sign of mass segregation, which could occur in self-gravity dominated systems such a globular clusters (Kim et al. 2015), could also cast doubt on the globular-cluster nature of Dra II, even though the existence of mass segregation, especially in a GC possibly in the midst of disruption, is not certain.

### 7.2 Is Dra II one of the faintest dwarf galaxies?

The top-left panel of Figure 20 showcases that Milky Way dwarf galaxies follow a reasonably well-defined luminosity-metallicity relation (see also, e.g., Kirby et al. 2013). For an extremely faint stellar system like Dra II, one would expect its metallicity to be very low ( $[\text{Fe}/\text{H}] \sim -2.5$ ) if it were a dwarf galaxy, which is compatible with our results using independently the CaHK photometry ( $[\text{Fe}/\text{H}]_{\text{CaHK}} = -2.7 \pm 0.1 \text{ dex}$ ) and spectroscopy of 3 low-RGB member stars ( $[\text{Fe}/\text{H}]_{\text{spectro}} = -2.43^{+0.41}_{-0.82} \text{ dex}$ ). Given the scatter and possible stochastic effects of the metallicity-luminosity relation of dwarf galaxies (Revaz & Jablonka 2018), Dra II is entirely compatible with this relation. Moreover, Dra II has a size larger than the vast majority of known Milky Way globular clusters and, in particular, it is several times more extended



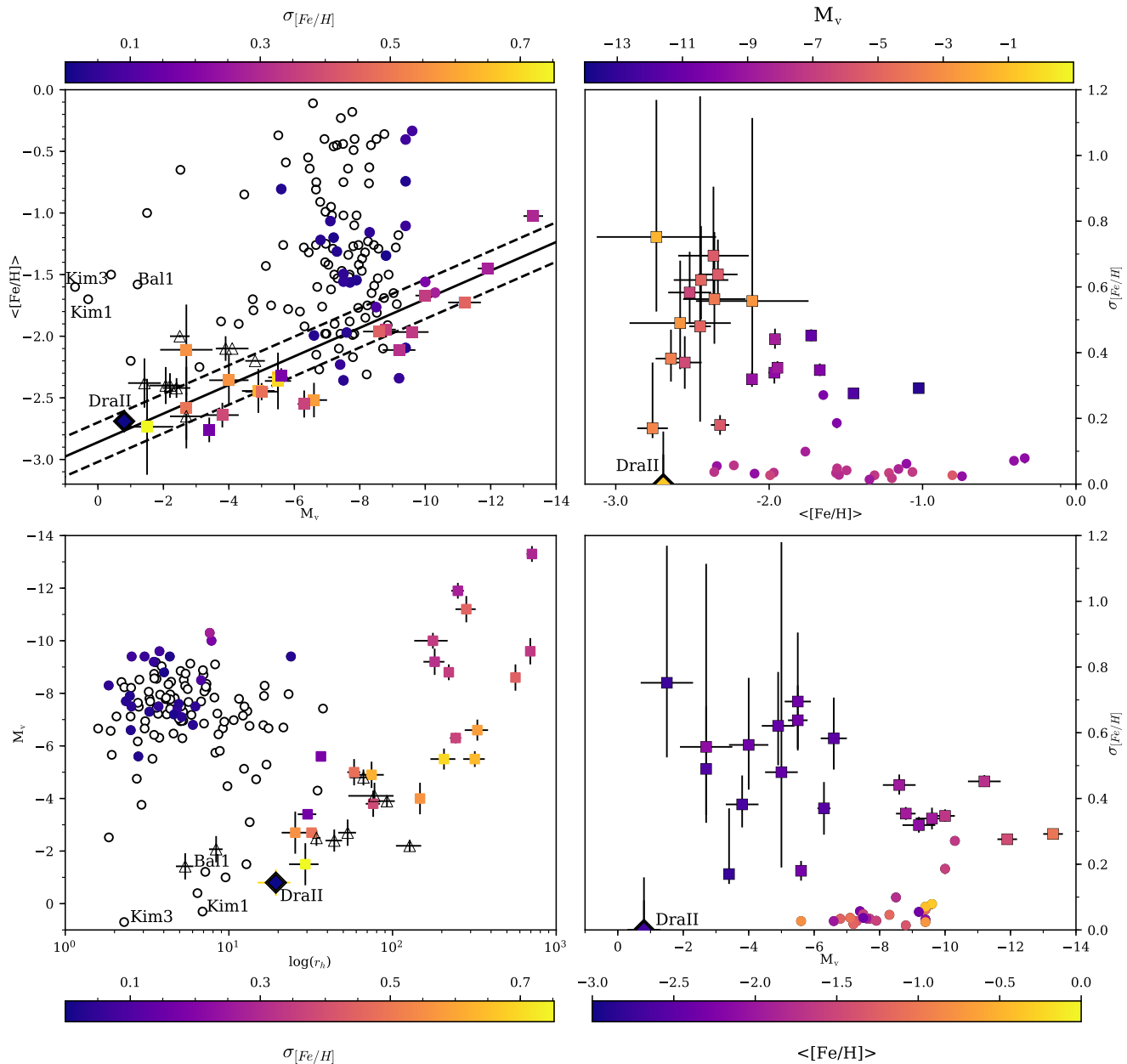


**Figure 20.** Comparison of Dra II with other GCs and dwarf galaxies of the Milky Way. Squares represent dwarf galaxies while circles represent globular clusters, and the diamond corresponds to Dra II. Triangles stand for recently discovered dwarf-galaxy candidates that await confirmation. Hollow markers correspond to systems for which no metallicity dispersion measurement can be found in the literature. The solid line in the top-left panel corresponds to the luminosity-metallicity relation of Kirby et al. (2013) for dwarf spheroidals and dwarf irregulars. Dashed lines represent the RMS about this relation, also taken from Kirby et al. (2013). Among the 123 globular clusters presented here, the properties of 116 were extracted from Harris (1996) catalog, revised in 2010. For the remaining ones (Kim 1, Kim 2, Kim 3, Laevens 1, Balbinot 1, Muñoz 1 and SMASH 1) parameters of the discovery publications were used (Kim & Jerjen (2015), Kim et al. (2015), Kim et al. (2016), Laevens et al. (2014), Balbinot et al. (2013), Muñoz et al. (2012) and Martin et al. (2016c)). Globular cluster metallicity spread measurements are taken from Willman & Strader (2012) and references therein: Carretta et al. (2006, 2007, 2009b, 2011), Cohen et al. (2010), Gratton et al. (2007), Johnson & Pilachowski (2010), and Marino et al. (2011). McConnachie (2012) and Willman & Strader (2012) are used to compile the properties of the dwarf galaxies represented here. The 18 dwarf galaxies represented here are: Bootes I (Belokurov et al. 2006; Norris et al. 2010), Canes Venatici I (Zucker et al. 2006b), Canes Venatici II (Sakamoto & Hasegawa 2006), Coma Berinices, Hercules, Leo IV and Segue I (Belokurov et al. 2007), Draco and Ursa Minor (Wilson 1955), Fornax (Shapley 1938b), Leo I and Leo II (Harrington & Wilson 1950), Pisces II (Belokurov et al. 2010), Sculptor (Shapley 1938a), Sextans (Irwin et al. 1990), Ursa Major I (Willman et al. 2005b), Ursa Major II (Zucker et al. 2006a), Willman I (Willman et al. 2005a). Their metallicity and metallicity spreads were drawn from Kirby et al. (2008), Kirby et al. (2010), Norris et al. (2010), Willman et al. (2011). The dwarf galaxy candidates discovered recently and shown on this figure are Bootes II (Koch & Rich 2014), DES1 (Luque et al. 2016; Conn et al. 2018), Eridanus III (Bechtol et al. 2015; Conn et al. 2018; Koposov et al. 2015b), Hyades II (Martin et al. 2015), Pegasus III (Kim & Jerjen 2015), Reticulum II and Horologium I (Koposov et al. 2015a), Segue II (Belokurov et al. 2009), and the most significant candidates of Drlica-Wagner et al. (2015) : Gru II, Tuc III, and Tuc IV.

than GCs of roughly the same luminosity and metallicity, as mentioned in the last section (bottom-left panel of Figure 20).

The inference on the metallicity dispersion of the satellite was performed through the spectroscopic analysis of 3 low-RGB member stars, and a new technique using the photometric CaHK metallicities of 41 stars. Though both methods do not resolve a significant metallicity dispersion, the final results do not rule it out for the system, because of the faintness and low number of the stars used in both analyses. Similarly, the velocity dispersion PDF of Dra II does not rule out a dynamical mass higher than expected from a globular cluster: if we use the Walker et al. (2009) equation 4 to estimate the dynamical mass, assuming a mass-to-light ratio of 2 that is typical for globular clusters (Bell & de Jong 2001), and the luminosity and half-light radius inferred in this work, a Dra II-like globular cluster should have a velocity dispersion around  $\sim 0.25 \text{ km s}^{-1}$ . It is therefore challenging to determine whether the satellite has a higher dynamical mass than traced by its stars alone, as even a velocity dispersion of the order of  $1 \text{ km s}^{-1}$  would indicate that Dra II has a DM halo.

Figure 9 highlights that there might be extended tidal structures around Dra II, consistent with the proper motion vector and the major-axis of the satellite. Its metallicity is still compatible with brighter dwarf galaxies following the metallicity-luminosity relation. Moreover, Peñarrubia, Navarro & McConnachie (2008) showed that the velocity dispersion of a disrupted dwarf galaxy tends to be lower than the original progenitor, consistent with the fact that Dra II appears to be dynamically cold. Could Dra II then be the final remnant of a brighter dwarf galaxy that lost 90 per cent of its mass through tidal interactions with the Milky Way? Such a disruption would not be surprising given the orbit of the satellite, with a pericenter of  $20.9^{+0.7}_{-0.9} \text{ kpc}$ .

### 7.3 Conclusion

The properties of Draco II tend to indicate that the satellite is a potentially disrupting dwarf galaxy, which could explain its total luminosity, metallicity, size, and relatively low velocity dispersion. The orbit of the satellite, constrained with Gaia PMs, shows that the satellite is very likely to be affected by tidal processes, which is backed up by potential tidal structures observed in the field. However, the impossibility, with our current dataset, to constrain the metallicity dispersion of Dra II casts a doubt of the nature of the satellite, which might well be a globular cluster observed at the very end of its disruption process. Even though challenging, obtaining high signal-to-noise spectra of the faint main-sequence stars of Dra II currently provides the only hope of unravelling the mystery still surrounding Dra II.

## 8 ACKNOWLEDGMENTS

RI, NL, and NFM gratefully acknowledge funding from CNRS/INSU through the Programme National Galaxies et Cosmologie and through the CNRS grant PICS07708. We gratefully thank the CFHT staff for performing the observations in queue mode. N. F. Martin acknowledges the Kavli Institute for Theoretical Physics in Santa Barbara and the

organizers of the ‘‘Cold Dark Matter 2018’’ program, during which some of this work was performed. This research was supported in part by the National Science Foundation under Grant No. NSF PHY11-25915. BPML gratefully acknowledges support from FONDECYT postdoctoral fellowship No. 3160510.

Based on observations obtained at the Canada-France-Hawaii Telescope (CFHT) which is operated by the National Research Council of Canada, the Institut National des Sciences de l’Univers of the Centre National de la Recherche Scientifique of France, and the University of Hawaii.

Some of the data presented herein were obtained at the W. M. Keck Observatory, which is operated as a scientific partnership among the California Institute of Technology, the University of California and the National Aeronautics and Space Administration. The Observatory was made possible by the generous financial support of the W. M. Keck Foundation. Furthermore, the authors wish to recognize and acknowledge the very significant cultural role and reverence that the summit of Maunakea has always had within the indigenous Hawaiian community. We are most fortunate to have the opportunity to conduct observations from this mountain.

The Pan-STARRS1 Surveys (PS1) have been made possible through contributions of the Institute for Astronomy, the University of Hawaii, the Pan-STARRS Project Office, the Max-Planck Society and its participating institutes, the Max Planck Institute for Astronomy, Heidelberg and the Max Planck Institute for Extraterrestrial Physics, Garching, The Johns Hopkins University, Durham University, the University of Edinburgh, Queen’s University Belfast, the Harvard-Smithsonian Center for Astrophysics, the Las Cumbres Observatory Global Telescope Network Incorporated, the National Central University of Taiwan, the Space Telescope Science Institute, the National Aeronautics and Space Administration under Grant No. NNX08AR22G issued through the Planetary Science Division of the NASA Science Mission Directorate, the National Science Foundation under Grant No. AST-1238877, the University of Maryland, and Eotvos Lorand University (ELTE).

This work has made use of data from the European Space Agency (ESA) mission *Gaia* (<https://www.cosmos.esa.int/gaia>), processed by the *Gaia* Data Processing and Analysis Consortium (DPAC, <https://www.cosmos.esa.int/web/gaia/dpac/consortium>). Funding for the DPAC has been provided by national institutions, in particular the institutions participating in the *Gaia* Multilateral Agreement.

## REFERENCES

- Balbinot E. et al., 2013, *ApJ*, 767, 101  
 Bechtol K. et al., 2015, *ApJ*, 807, 50  
 Bell E. F., de Jong R. S., 2001, *ApJ*, 550, 212  
 Bellazzini M. et al., 2008, *AJ*, 136, 1147  
 Belokurov V. et al., 2010, *ApJ*, 712, L103  
 —, 2009, *MNRAS*, 397, 1748  
 —, 2007, *ApJ*, 654, 897  
 —, 2006, *ApJ*, 647, L111  
 Bernard E. J. et al., 2014, *MNRAS*, 442, 2999  
 Boulade O. et al., 2003, 4841, 72  
 Bovy J., 2015, *ApJS*, 216, 29  
 Brown T. M. et al., 2014, 85, 493  
 Bullock J. S., Boylan-Kolchin M., 2017, *ARAA*, 55, 343  
 Carretta E., Bragaglia A., Gratton R., D’Orazi V., Lucatello S., 2009a, *A&A*, 508, 695  
 Carretta E., Bragaglia A., Gratton R. G., Leone F., Recio-Blanco A., Lucatello S., 2006, *A&A*, 450, 523  
 Carretta E. et al., 2010, *ApJ*, 714, L7  
 —, 2009b, *A&A*, 505, 117  
 —, 2007, *A&A*, 464, 967  
 Carretta E., Lucatello S., Gratton R. G., Bragaglia A., D’Orazi V., 2011, *A&A*, 533, A69  
 Chambers K. C. et al., 2016, *ArXiv e-prints*  
 Cohen J. G., Kirby E. N., Simon J. D., Geha M., 2010, *ApJ*, 725, 288  
 Conn B. C., Jerjen H., Kim D., Schirmer M., 2018, *ApJ*, 852, 68  
 Dotter A., Chaboyer B., Jevremović D., Kostov V., Baron E., Ferguson J. W., 2008, *ApJS*, 178, 89  
 Drlica-Wagner A. et al., 2015, *ApJ*, 813, 109  
 Faber S. M. et al., 2003, 4841, 1657  
 Fritz T. K., Battaglia G., Pawlowski M. S., Kallivayalil N., van der Marel R., Sohn T. S., Brook C., Besla G., 2018, *ArXiv e-prints*  
 Gaia Collaboration, Brown A. G. A., Vallenari A., Prusti T., de Bruijne J. H. J., Babusiaux C., Bailer-Jones C. A. L., 2018a, *ArXiv e-prints*  
 Gaia Collaboration et al., 2018b, *ArXiv e-prints*  
 Gratton R. G. et al., 2007, *A&A*, 464, 953  
 Harrington R. G., Wilson A. G., 1950, *PASP*, 62, 118  
 Harris W. E., 1996, *AJ*, 112, 1487  
 Hastings W. K., 1970, *Biometrika*, 97  
 Ibata R., Sollima A., Nipoti C., Bellazzini M., Chapman S. C., Dalessandro E., 2011, *ApJ*, 738, 186  
 Ibata R. A. et al., 2014, *ApJ*, 780, 128  
 Innanen K. A., Harris W. E., Webbink R. F., 1983, *AJ*, 88, 338  
 Irwin M., Lewis J., 2001, *New Astronomy Review*, 45, 105  
 Irwin M. J., Bunclark P. S., Bridgeland M. T., McMahon R. G., 1990, *MNRAS*, 244, 16P  
 Johnson C. I., Pilachowski C. A., 2010, *ApJ*, 722, 1373  
 Kim D., Jerjen H., 2015, *ApJ*, 799, 73  
 Kim D., Jerjen H., Mackey D., Da Costa G. S., Milone A. P., 2016, *ApJ*, 820, 119  
 Kim D., Jerjen H., Milone A. P., Mackey D., Da Costa G. S., 2015, *ApJ*, 803, 63  
 Kirby E. N., Cohen J. G., Guhathakurta P., Cheng L., Bullock J. S., Gallazzi A., 2013, *ApJ*, 779, 102  
 Kirby E. N. et al., 2010, *ApJS*, 191, 352  
 Kirby E. N., Simon J. D., Geha M., Guhathakurta P., Frebel A., 2008, *ApJ*, 685, L43  
 Koch A., Rich R. M., 2014, *ApJ*, 794, 89  
 Koposov S. et al., 2007, *ApJ*, 669, 337  
 Koposov S. E., Belokurov V., Torrealba G., Evans N. W., 2015a, *ApJ*, 805, 130  
 Koposov S. E. et al., 2015b, *ApJ*, 811, 62  
 Koposov S. E., Yoo J., Rix H.-W., Weinberg D. H., Macciò A. V., Escudé J. M., 2009, *ApJ*, 696, 2179  
 Laevens B. P. M. et al., 2015, *ApJ*, 813, 44  
 —, 2014, *ApJ*, 786, L3  
 Leaman R. et al., 2013, *ApJ*, 767, 131  
 Luque E. et al., 2016, *MNRAS*, 458, 603  
 Marino A. F. et al., 2011, *A&A*, 532, A8  
 Martin N. F., Collins M. L. M., Longeard N., Tollerud E., 2018, *ArXiv e-prints*  
 Martin N. F., de Jong J. T. A., Rix H.-W., 2008, *ApJ*, 684, 1075  
 Martin N. F. et al., 2016a, *MNRAS*, 458, L59  
 Martin N. F., Ibata R. A., Chapman S. C., Irwin M., Lewis G. F., 2007, *MNRAS*, 380, 281  
 Martin N. F. et al., 2016b, *ApJ*, 833, 167  
 —, 2016c, *ApJ*, 830, L10  
 —, 2015, *ApJ*, 804, L5  
 McConnachie A. W., 2012, *AJ*, 144, 4  
 McConnachie A. W., Côté P., 2010, *ApJ*, 722, L209  
 McLaughlin D. E., van der Marel R. P., 2005, *ApJS*, 161, 304  
 Muñoz R. R., Geha M., Côté P., Vargas L. C., Santana F. A., Stetson P., Simon J. D., Djorgovski S. G., 2012, *ApJ*, 753, L15  
 Norris J. E., Wyse R. F. G., Gilmore G., Yong D., Frebel A., Wilkinson M. I., Belokurov V., Zucker D. B., 2010, *ApJ*, 723, 1632  
 Peñarrubia J., Navarro J. F., McConnachie A. W., 2008, *ApJ*, 673, 226  
 Revaz Y., Jablonka P., 2018, *ArXiv e-prints*  
 Romani R. W., Weinberg M. D., 1991, in *Astronomical Society of the Pacific Conference Series*, Vol. 13, The Formation and Evolution of Star Clusters, Janes K., ed., pp. 443–445  
 Sakamoto T., Hasegawa T., 2006, *ApJ*, 653, L29  
 Schlafly E. F., Finkbeiner D. P., 2011, *ApJ*, 737, 103  
 Schlegel D. J., Finkbeiner D. P., Davis M., 1998, *ApJ*, 500, 525  
 Shapley H., 1938a, *Harvard College Observatory Bulletin*, 908, 1  
 —, 1938b, *Nature*, 142, 715  
 Simon J. D., 2018, *ArXiv e-prints*  
 Simon J. D., Geha M., 2007, *ApJ*, 670, 313  
 Starkenburg E. et al., 2010, *A&A*, 513, A34  
 —, 2017, *MNRAS*, 471, 2587  
 The Dark Energy Survey Collaboration, 2005, *ArXiv Astrophysics e-prints*  
 Tonry J. L. et al., 2012, *ApJ*, 750, 99  
 Vargas L. C., Geha M., Kirby E. N., Simon J. D., 2013, *ApJ*, 767, 134  
 Walker M. G., Mateo M., Olszewski E. W., Peñarrubia J., Wyn Evans N., Gilmore G., 2009, *ApJ*, 704, 1274  
 Willman B. et al., 2005a, *AJ*, 129, 2692  
 —, 2005b, *ApJ*, 626, L85  
 Willman B., Geha M., Strader J., Strigari L. E., Simon J. D., Kirby E., Ho N., Warren A., 2011, *AJ*, 142, 128

**Table 2.** Properties of our spectroscopic sample. Stars A, B and C have a radial velocity of respectively -356.4, -306.2 and -330.5 km s<sup>-1</sup> and are indicated in the column "Member".

RA (deg)	DEC (deg)	$g_0$	$i_0$	$C\alpha HK$	$v_r$ (km s <sup>-1</sup> )	$\mu_{\alpha}^*$ (mas.yr <sup>-1</sup> )	$\mu_{\delta}$ (mas.yr <sup>-1</sup> )	$\mu_6$ (mas.yr <sup>-1</sup> )	S/N	[Fe/H] <sub>CaHK</sub>	$P_{mem}$	Member	Time
238.34537500	+64.57397222	19.07 ± 0.01	18.62 ± 0.01	19.95 ± 0.01	-125.8 ± 1.3 -125.0 ± 1.5 -129.3 ± 2.9	-4.44 ± 0.45	-4.02 ± 0.47	23.2	—	—	0.00	N	Averaged 2015 2016
238.50220833	+64.58488889	20.05 ± 0.01	19.66 ± 0.01	20.78 ± 0.01	-244.0 ± 3.1	-4.27 ± 0.86	0.74 ± 0.93	9.9	-1.03 ± 0.15	0.37	0.37	N	2016
238.48954167	+64.58458333	20.59 ± 0.01	19.98 ± 0.01	21.63 ± 0.03	-411.9 ± 5.2	-2.84 ± 1.44	-5.55 ± 1.24	6.9	-1.07 ± 0.13	0.00	0.00	N	2016
238.40962500	+64.61827778	20.85 ± 0.01	20.61 ± 0.01	21.28 ± 0.02	-328.4 ± 8.8	-0.04 ± 3.08	2.54 ± 2.04	4.6	-2.50 ± 0.46	0.88	0.88	Y	2016
238.13162500	+64.56455556	18.85 ± 0.01	18.29 ± 0.01	19.83 ± 0.01	-137.2 ± 1.7	-7.08 ± 0.32	1.52 ± 0.33	25.6	—	0.03	0.03	N	2016
238.32470833	+64.59466667	18.98 ± 0.01	18.89 ± 0.01	19.36 ± 0.01	194.0 ± 8.1	33.07 ± 0.47	42.0 ± 0.46	17.5	—	0.00	0.00	N	2016
238.29208333	+64.56011111	19.36 ± 0.01	18.80 ± 0.01	20.05 ± 0.01	-341.6 ± 0.9 -340.6 ± 1.1 -343.7 ± 1.5	1.11 ± 0.50	0.99 ± 0.49	20.5	-2.42 ± 0.17	0.86	0.86	Y	Averaged 2015 2016
238.22750000	+64.57172222	19.83 ± 0.01	19.38 ± 0.01	20.35 ± 0.01	-341.9 ± 1.7 -338.3 ± 2.8 -344.1 ± 2.2	1.64 ± 0.85	-0.14 ± 0.87	17.3	-2.93 ± 0.23	0.18	0.18	Y	Averaged 2015 2016
238.17570833	+64.57013889	19.84 ± 0.01	19.34 ± 0.01	20.44 ± 0.01	-346.9 ± 1.6 -345.1 ± 2.6 -348.0 ± 2.0	1.45 ± 0.68	0.92 ± 0.73	15.1	-2.57 ± 0.22	0.83	0.83	Y	Averaged 2015 2016
238.22337500	+64.55341667	20.07 ± 0.01	19.69 ± 0.01	20.53 ± 0.01	-341.9 ± 2.2 -341.0 ± 2.5 -345.4 ± 4.9	1.15 ± 0.84	0.46 ± 0.93	13.3	-2.93 ± 0.23	0.93	0.93	Y	Averaged 2015 2016
238.07675000	+64.59608333	20.52 ± 0.01	19.25 ± 0.01	22.50 ± 0.05	-95.9 ± 2.2 -94.2 ± 3.2 -97.6 ± 3.1	0.09 ± 0.73	-7.85 ± 0.80	13.2	—	0.00	0.00	N	Averaged 2015 2016
238.21795833	+64.59575000	20.68 ± 0.01	20.45 ± 0.01	21.06 ± 0.02	-343.5 ± 4.6 -343.6 ± 14.0 -343.5 ± 4.9	3.81 ± 1.66	1.45 ± 1.94	7.7	-2.77 ± 0.31	0.99	0.99	Y	Averaged 2015 2016
238.19866667	+64.54908333	20.71 ± 0.01	20.41 ± 0.01	21.13 ± 0.02	-347.5 ± 4.8	1.91 ± 1.73	0.40 ± 2.02	7.0	-2.72 ± 0.38	0.14	0.14	Y	2016
238.15762500	+64.54386111	20.74 ± 0.01	20.49 ± 0.01	21.11 ± 0.02	-346.1 ± 6.9	-0.42 ± 1.84	2.88 ± 2.03	7.2	-2.91 ± 0.30	0.98	0.98	Y	2016
238.29766667	+64.58597222	20.90 ± 0.01	20.59 ± 0.01	21.36 ± 0.02	-349.7 ± 6.2	—	—	6.6	-2.41 ± 0.44	0.20	0.20	Y	2016
238.22362500	+64.56244444	20.94 ± 0.01	20.65 ± 0.01	21.39 ± 0.02	-349.7 ± 5.5	—	—	6.6	-2.48 ± 0.38	0.87	0.87	Y	2016
238.25691667	+64.54466667	21.05 ± 0.01	20.78 ± 0.01	21.50 ± 0.02	-340.0 ± 8.4	—	—	5.4	-2.49 ± 0.39	0.98	0.98	Y	2016
238.18845833	+64.58144444	21.62 ± 0.01	21.31 ± 0.01	22.07 ± 0.03	-336.3 ± 12.8	—	—	3.6	-2.76 ± 0.46	0.99	0.99	Y	2016
238.27908333	+64.56091667	22.71 ± 0.02	21.55 ± 0.01	24.11 ± 0.17	-206.3 ± 5.4	—	—	3.3	-2.35 ± 0.60	0.00	0.00	N	2016
238.00450000	+64.55847222	18.82 ± 0.01	18.22 ± 0.01	19.91 ± 0.01	-47.2 ± 1.6	1.63 ± 0.30	-2.54 ± 0.33	25.9	—	0.39	0.39	N	2016
238.00004167	+64.57619444	20.37 ± 0.01	18.83 ± 0.01	22.56 ± 0.05	-66.7 ± 2.2	-1.79 ± 0.53	-10.54 ± 0.53	21.6	—	0.00	0.00	N	2016
238.05320833	+64.52075000	20.87 ± 0.01	19.56 ± 0.01	22.96 ± 0.07	-47.4 ± 3.4	-6.80 ± 0.98	-2.43 ± 0.97	12.8	—	0.00	0.00	N	2016
238.05975000	+64.55613889	22.04 ± 0.01	20.94 ± 0.01	23.80 ± 0.15	-253.1 ± 7.1	—	—	5.7	—	0.00	0.00	N	2016
238.52529167	+64.59861111	16.73 ± 0.01	16.18 ± 0.01	17.74 ± 0.0	3.6 ± 0.9	-7.16 ± 0.09	-6.06 ± 0.09	65.4	—	0.00	0.00	N	2016
238.39033333	+64.63200000	17.60 ± 0.01	16.33 ± 0.01	19.75 ± 0.01	-30.9 ± 1.2	-4.37 ± 0.10	-2.53 ± 0.10	52.8	—	0.00	0.00	N	2016
238.34487500	+64.58811111	17.20 ± 0.01	16.60 ± 0.01	18.34 ± 0.0	-41.8 ± 1.2	-6.68 ± 0.13	14.34 ± 0.14	57.4	—	0.00	0.00	N	2016
238.27975000	+64.56305556	16.93 ± 0.01	16.20 ± 0.01	18.13 ± 0.0	-52.0 ± 1.0	-13.07 ± 0.19	-0.92 ± 0.17	66.4	-1.12 ± 0.09	0.21	0.21	N	2016
238.23100000	+64.59677778	17.76 ± 0.01	17.12 ± 0.01	18.94 ± 0.0	-4.1 ± 0.9	0.92 ± 0.16	-2.94 ± 0.16	47.7	—	0.11	0.11	N	2016
238.11125000	+64.57577778	17.43 ± 0.01	16.73 ± 0.01	18.73 ± 0.0	-68.8 ± 0.9	-4.60 ± 0.12	-2.21 ± 0.13	50.4	—	0.56	0.56	N	2016
238.01183333	+64.53602778	17.96 ± 0.01	17.37 ± 0.01	19.09 ± 0.01	-76.7 ± 1.3	-0.77 ± 0.18	-3.42 ± 0.18	37.8	—	0.00	0.00	N	2016
238.56645417	+64.50524722	19.00 ± 0.01	18.42 ± 0.01	20.03 ± 0.01	-225.2 ± 2.3	-2.14 ± 0.38	-0.71 ± 0.41	5.5	—	0.02	0.02	N	2015

**Table 3.** Properties of our spectroscopic sample. Stars A, B and C have a radial velocity of respectively -356.4, -306.2 and -330.5 km s<sup>-1</sup> and are indicated in the column "Member".

RA (deg)	DEC (deg)	$g_0$	$i_0$	$CaHK$	$v_r$ (km s <sup>-1</sup> )	$\mu_{\alpha}^*$ (mas.yr <sup>-1</sup> )	$\mu_{\delta}$ (mas.yr <sup>-1</sup> )	S/N	[Fe/H] <sub>CaHK</sub>	$P_{mem}$	Member	Time
238.51061250	+64.55532500	19.88 ± 0.01	18.28 ± 0.01	22.15 ± 0.04	-53.2 ± 1.5	6.87 ± 0.40	-6.51 ± 0.42	6.3	—	0.00	N	2015
238.54619167	+64.52975556	20.39 ± 0.01	19.99 ± 0.01	21.11 ± 0.02	-165.9 ± 8.8	-2.78 ± 1.73	-0.87 ± 1.18	3.0	-1.15 ± 0.13	0.00	N	2015
238.55823750	+64.56613611	21.74 ± 0.01	20.00 ± 0.01	23.83 ± 0.14	-39.9 ± 4.7	-3.41 ± 2.63	-4.42 ± 2.37	5.4	—	0.00	N	2015
238.41302083	+64.57990000	22.32 ± 0.01	21.37 ± 0.01	23.82 ± 0.14	-356.4 ± 5.5	—	—	3.1	-1.34 ± 0.53	0.00	N	2015
238.42835417	+64.57927222	22.41 ± 0.01	21.81 ± 0.02	23.06 ± 0.07	-306.2 ± 14.9	—	—	3.3	-2.68 ± 0.63	0.00	N	2015
238.15138333	+64.60540000	19.44 ± 0.01	18.92 ± 0.01	20.03 ± 0.01	-337.6 ± 2.7	0.90 ± 0.52	1.08 ± 0.54	4.1	-2.82 ± 0.24	0.03	Y	2015
238.22609167	+64.59788333	19.57 ± 0.01	18.53 ± 0.01	21.26 ± 0.02	-84.5 ± 1.6	-1.76 ± 0.45	-1.74 ± 0.46	8.6	—	0.00	N	2015
238.21103333	+64.57847778	20.07 ± 0.01	18.59 ± 0.01	22.24 ± 0.04	-3.5 ± 1.6	-3.22 ± 0.53	-13.88 ± 0.55	6.7	—	0.00	N	2015
238.20966667	+64.61985278	20.26 ± 0.01	19.38 ± 0.01	21.58 ± 0.02	-182.3 ± 4.9	-6.00 ± 0.88	3.11 ± 0.98	20.7	-1.62 ± 0.13	0.00	N	2015
238.25460417	+64.54189167	20.63 ± 0.01	20.05 ± 0.01	21.66 ± 0.03	9.4 ± 4.2	-5.38 ± 1.27	2.03 ± 1.44	3.6	-1.02 ± 0.15	0.00	N	2015
238.28841250	+64.58975000	21.39 ± 0.01	19.68 ± 0.01	23.71 ± 0.12	-61.7 ± 2.3	-8.05 ± 1.42	1.98 ± 1.49	5.1	—	0.00	N	2015
238.18912917	+64.55407222	22.21 ± 0.01	21.67 ± 0.02	22.96 ± 0.07	-330.5 ± 5.5	—	—	3.6	-2.53 ± 0.51	0.00	N	2015
238.03618333	+64.57617500	21.00 ± 0.01	20.73 ± 0.01	21.40 ± 0.02	-325.7 ± 8.9	2.71 ± 2.97	0.26 ± 3.51	3.1	-2.90 ± 0.33	0.95	Y	2015
238.51431587	+64.57347835	17.98 ± 0.01	17.49 ± 0.01	18.89 ± 0.0	-79.9 ± 1.1	-6.51 ± 0.19	0.49 ± 0.20	13.1	—	0.00	N	2015
238.49718375	+64.51780965	18.14 ± 0.01	16.31 ± 0.01	20.26 ± 0.01	-11.9 ± 1.1	-68.75 ± 0.13	-42.7 ± 0.13	14.7	—	0.00	N	2015
238.43973971	+64.56761491	18.07 ± 0.01	16.91 ± 0.01	20.04 ± 0.01	-64.2 ± 1.3	6.83 ± 0.17	-6.09 ± 0.17	15.1	—	0.00	N	2015
238.21533400	+64.60644630	15.42 ± 0.01	14.99 ± 0.01	16.29 ± 0.0	-54.3 ± 1.1	-14.42 ± 0.05	-5.44 ± 0.05	96.1	—	0.00	N	2015
238.18480597	+64.61537726	17.88 ± 0.01	17.25 ± 0.01	19.09 ± 0.01	-35.1 ± 1.3	-5.66 ± 0.17	-4.63 ± 0.17	25.8	—	0.03	N	2015
238.12209840	+64.60199650	18.92 ± 0.01	16.98 ± 0.01	21.15 ± 0.02	-0.9 ± 1.2	-1.69 ± 0.20	11.09 ± 0.20	8.9	—	0.00	N	2015
238.11487862	+64.60882637	17.89 ± 0.01	16.96 ± 0.01	19.60 ± 0.01	-123.9 ± 1.2	4.81 ± 0.15	-22.05 ± 0.15	11.8	—	0.00	N	2015

- Willman B., Strader J., 2012, *AJ*, 144, 76  
Wilson A. G., 1955, *PASP*, 67, 27  
York D. G. et al., 2000, *AJ*, 120, 1579  
Youakim K. et al., 2017, *MNRAS*, 472, 2963  
Zucker D. B. et al., 2006a, *ApJ*, 650, L41  
—, 2006b, *ApJ*, 643, L103